Development and Experimental Evaluation
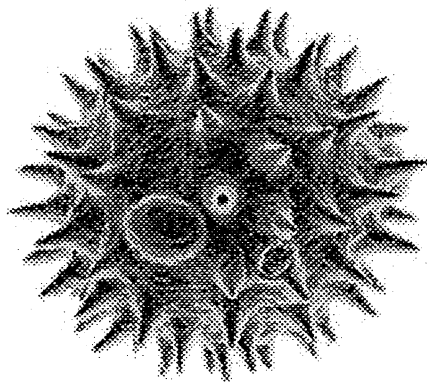## of an Optical Sensor
for Aerosol Particle Characterization

Master's Thesis
by
Gabriel Somesfalean

Supervisors

Professor Sune Svanberg
M.Sc. Jonas Sandsten

Picture on previous page: *Anisodontea Bush Pollen* (2000 magnification)

Abstract

A sensor for individual aerosol particle characterization, based on a single-mode semiconductor laser coupled to an external cavity is presented. The light emitting semiconductor laser acts as a sensitive optical detector itself, and the whole system has the advantage of using conventional optical components and providing a compact set-up.

Aerosol particles moving through the sensing volume, which is located in the external cavity of a semiconductor laser, scatter and absorb light. Thereby they act as small disturbances on the electromagnetic field inside the dynamic multi-cavity laser system. From the temporal variation of the output light intensity, information about the number, velocity, size, and refractive index of the aerosol particles can be derived.

The diffracted light in the near-forward scattering direction is collected and Fourier-transformed by a lens, and subsequently imaged on a CCD camera. The recorded Fraunhofer diffraction pattern provides information about the projected area of the scattering particle, and can thus be used to determine the size and the shape of aerosol particles.

The sensor has been tested on fibers which are of interest in the field of working environment monitoring. The recorded output intensity variation has been analysed, and the relationship between the shape and the size of each fibre, and the resulting scattering profiles has been investigated.

A simple one-dimensional model for the optical feedback variation due to the light-particle interaction in the external cavity is also discussed.

Table of contents

1. Introduction and theoretical approach

1.1 Introductory overview

Atmospheric particles have a great impact on the climate of our planet as well as on our health. Outlets to the atmosphere have resulted in many environmental alarms such as global warming, depletion of the stratospheric ozone layer, and serious urban pollution, just to mention a few. It has been estimated that world-wide, nearly one billion people in urban environments are continuously being exposed to health hazards due to air pollutants [1]. Getting more knowledge about aerosol particles, and trying to understand the effects of various natural and man-made aerosols can help us to protect our environment and to fight against pollution.

The characterization of airborne particles is critical in the study of a wide range of fields including monitoring of industrial emissions and ambient air quality, as well as research on e.g. cloud and fog formation. In recent years, increasing emphasis has been laid on indoor aerosols, since people on the average spend 80-90% of their time indoors [2]. Health concerns have often driven the technology for detecting and quantifying airborne particles.

There are two basic approaches to the measurement of aerosol particles [2]. The traditional approach is to sample the particles onto a filter. This method, called *extractive*, generally relies on experts to examine the filters under microscope in a laboratory, which is a time consuming procedure that usually cannot be carried out on site.
The other approach is to sample the aerosol directly into a real-time, dynamic measuring instrument. The major advantage of this measurement technique, called *in situ*, is that the data are immediately available. The disadvantage, however, is that *in situ* aerosol measurement systems are generally expensive.
One way to make *in situ* detection of particles is by collecting scattered light from them. In optical aerosol measurement instruments the interaction of aerosol particles with the incident light serves as a basis for the real time measurement. High reliability and accuracy of the measurement, possibility of remote sensing and detection of the particles in their airborne state are some of the main advantages of this scattering technique [3,4].

The layout of this work follows these lines:
In Chapter 1 a brief theoretical introduction to the field of semiconductor lasers and of light scattering by particles is given. Sect. 1.3.2 is specially focused on semiconductor lasers coupled to an external cavity, while Sect. 1.5 presents a simple model for the light-particle interaction inside the external cavity of such a laser system. Sect. 1.6 deals with aerosols and aerosol measurement.
Chapter 2 describes the design of the aerosol detector and presents its consisting components. Some experimental findings about the operation of the external cavity system and the optics are also given.
In Chapter 3 the results of the performed experimental measurements are presented and evaluated. In Sect. 3.3 a brief diagnostic investigation of the sensor characteristics is done.
In the fourth chapter the measurements and the results are discussed, and a few improvement suggestions are given. Finally, Sect. 4.4 summarises the conclusions.

At the end, three Appendices have been attached, regarding experimental details and derivation of some results presented in the experiment evaluation.

1.2 The purpose of this project

This project was part of the research done by the Molecular Spectroscopy Group at the Atomic Physics Department at Lund Institute of Technology. The research activity of the group is oriented towards optical monitoring of indoor working environments and outdoor pollution.

The purpose of this project was to develop a device for *in situ* detection of micrometer-size aerosol particles. Besides measurement of particle concentration and size, it should provide information on the shape of aerosol particles in order to render possible their identification. The light scattering technique was chosen because of its advantages, including rapid, continuous and sensitive detection, and avoidance of physical contact with the particles.
The instrument is intended to be used for single-particle detection, corresponding to a so-called *optical particle counter* (OPC) [2], but it may as well be applied for light scattering measurements of a small assembly of particles.
A primary goal was to evaluate whether a semiconductor laser coupled to an external cavity can be employed as an aerosol particle monitor. Due to their many benefits, such as compactness, efficiency, reliability, and low cost, semiconductor lasers are light sources well suited for spectroscopy and metrology [5]. They can realise compact sensor heads in portable instruments, easy to use when making aerosol measurements in field environments.

An external cavity is formed by placing an external reflector in front of the laser, whereby optical feedback of radiation is returned back into the laser cavity.
The basis of the prototype optical sensor is *active scattering*, which means that the sensing volume is located inside the laser resonator. The aerosol particles move through the passive external cavity and interact with the electromagnetic field by scattering and absorbing the light. They act as small, short-time disturbances on the steady-state of the system, causing changes of the output light intensity. Information about the aerosol particles can be obtained by processing the resulting output intensity variations. Used in this way, the semiconductor laser performs as an extremely sensitive device.

Additionally, diffracted light in the near-forward scattering direction is collected and imaged on a CCD camera. The pattern of scattered light forms a unique "fingerprint" characteristic for each type of aerosol particle, and can thus be used for identification purposes [6].

This is a pilot study, and the main practical concern during this initial stage of the work was to get a better understanding of the operation of a semiconductor laser with an external cavity. This is a prerequisite, because without a functioning external cavity no scattering measurements can be done. Consequently, extensive experimental tests have been performed, and a theoretical approach to describe the light-particle interaction in the external cavity through a simple one-dimensional model is also proposed.
A thorough evaluation and calibration of the aerosol particle sensor, as well as development of the technique and testing on the field, remain still to be done.

## 1.3 Theory of the semiconductor laser with an external cavity

In order to understand and fully control the operation of the semiconductor laser when employed as a particle sensor, the properties of this opto-electronic device have been studied theoretically and experimentally. The first part of this section is intended to give a concise introduction into the field of solid-state semiconductor lasers. The second part is dealing with semiconductor lasers with an external cavity. Some useful expressions concerning the emission spectrum and the steady-state characterization, as well as for the optical output power are also derived.

1.3.1 The laser diode

The semiconductor laser, alternatively known as the laser diode (LD), was invented in 1962, soon after the development of the light-emitting diode (LED) [3].

A laser (the term is an acronym for Light Amplification by Stimulated Emission of Radiation) consists of a light amplifying medium (active medium), where significant amount of stimulated emission occurs, and of a resonator cavity. As for the semiconductor laser, it is essentially a pn-junction combined with an optical resonator.

A first condition for lasing to occur is that the population of the excited state (conduction band) is higher than that of the ground state (valence band). The system is then operated in a non-equilibrium state called *population inversion* [7]. Energy has to be supplied to the system by pumping. In the case of a laser diode, charge carriers are injected into the pn-junction by applying a bias voltage in the forward direction. Stimulated light emission with a photon energy corresponding to the band gap between the conduction band and the valence band will result upon the recombination of electrons and holes (see the energy-level diagram shown in Fig. 1.1).
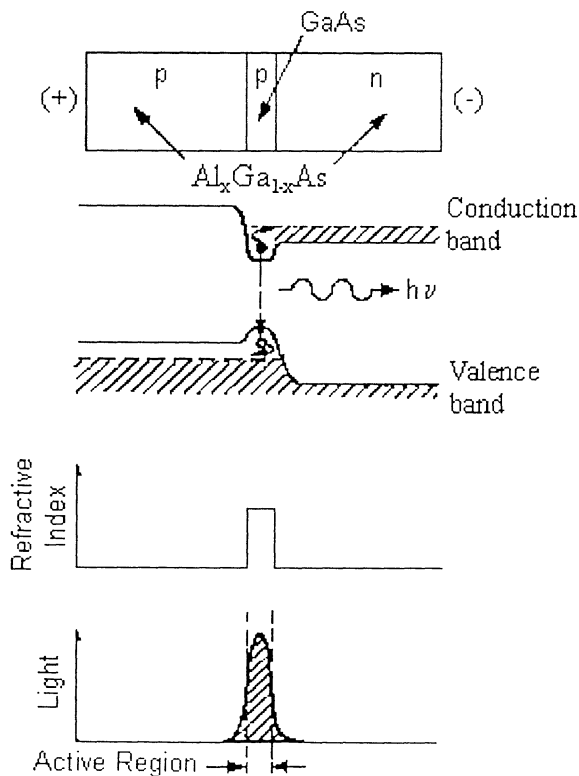
Fig. 1.1 *Structure and characteristics of a laser diode. (Here a double hetero-junction type.)*

The double-heterojunction (DH) laser diode was the first semiconductor laser configuration capable of continuous operation at room temperature, and it has become the prevalent type for most applications today [8,9]. It consists of a thin layer of undoped semiconductor (GaAs) sandwiched between p-doped and n-doped regions of another semiconductor with a slightly larger bandgap energy ($Al_xGa_{1-x}As$). This design leads to an efficient confinement of both the charge carriers and the optical field to the so-called *active region* (see Fig. 1.1).

A second condition for lasing consists in light amplification through optical feedback. A *Fabry-Perot resonator cavity* is created by cleaving the ends of the semiconductor crystal to form two parallel reflective surfaces.

In a Fabry-Perot cavity, if a multiple whole number of half-wavelengths fit between the two end planes, reinforced and coherent light will be reflected back and forth within the resonator cavity [7]. Constructive interference allows creation of standing waves corresponding to so-called *resonator modes*. Thus, the length L_D of the diode cavity must satisfy the condition

$$L_D = m\left(\frac{\lambda}{2n}\right) \quad \Rightarrow m\lambda = 2nL_D,$$

(1.1)

where m is an integer representing the order of the longitudinal mode, and n is the refractive index of the active region corresponding to the wavelength λ. Fig. 1.2 shows schematically the propagation of plane waves in a Fabry-Perot resonator.

The separation between two neighbouring longitudinal modes, $\Delta\lambda = \lambda_m - \lambda_{m+1}$, can be derived by differentiating Eq. (1.1) with respect to λ, and we obtain

$$\Delta\lambda = \frac{\lambda^2}{2nL_D} \quad \Rightarrow \Delta\omega_D = \frac{\pi c}{nL_D}.$$

(1.2)

Here the dispersion was neglected ($dn/d\lambda = 0$).

Laser oscillation will start from the noise of the spontaneous emission at the mode for which the amplification is greatest, i.e. at the wavelength with the maximum gain. The *laser threshold* is the characteristic level of the pumping at which lasing starts. Below threshold the laser emits weak, incoherent and spectrally broad radiation. The semiconductor laser is then comparable to a light-emitting diode. Above threshold, intense, coherent and spectrally sharp emission is observed. At *single-mode emission* the other longitudinal modes will be effectively suppressed.
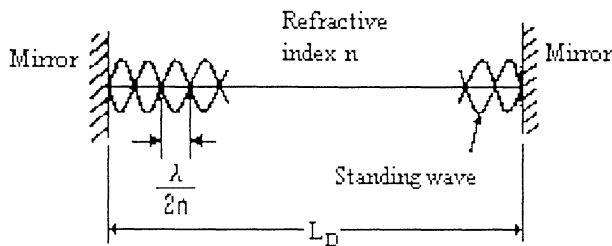

Fig. 1.2 *Standing wave in a laser resonator.*

At the threshold for lasing the gain, defined as the incremental optical energy flux per unit length, satisfies the condition that an electromagnetic wave makes a complete round trip of the cavity without attenuation [10]. It yields

$$R_1 R_2 \cdot \exp\left[2(\Gamma g - \alpha_i)L_D\right] = 1,$$ (1.3)

where Γ is the confinement factor accounting for the ratio of the light intensity within the active layer to the total light intensity inside the laser cavity [11], g is the gain at the lasing mode, α_i represents the intrinsic losses per unit length due to material absorption and scattering, L_D is the diode cavity length, and R_1 and R_2 are the reflectivities of the both ends of the cavity, respectively. The threshold condition above can be rewritten as a relation for the required gain at threshold

$$g = g_{th} = \frac{1}{\Gamma}\left(\alpha_i + \frac{1}{2L_D}\ln\frac{1}{R_1 R_2}\right) = \frac{1}{\Gamma}(\alpha_i + \alpha_M).$$ (1.4)

This expression means that the condition for laser oscillation to occur is that the amplification must compensate for the intrinsic losses α_i and the transmission (or mirror) losses α_M. Hence, a light wave inside the resonator is amplified only if the optical gain, related to the stimulated emission, is sufficiently large.

The field equation. The steady-state and dynamic characteristics of a laser are usually described by rate equations or by a field equation approach [8,11,12]. In the following, a simple derivation of the rate equation for the photons is given, which is then related to the field equation for the electromagnetic wave inside the cavity.

The change in the photon number S inside the cavity, within the considered oscillating mode, is caused by stimulated emission, absorption and spontaneous emission. The rate of change of the photon number can therefore be described by

$$\frac{dS}{dt} = R_{st}S - \frac{1}{\tau_{ph}}S + R_{sp},$$ (1.5)

where R_{st} corresponds to the number of photons generated per unit of time due to stimulated emission, $1/\tau_{ph}$ is the rate of loss related to the photon lifetime τ_{ph}, and R_{sp} denotes the effective spontaneous emission coefficient.

The stimulated emission rate is related to the gain coefficient according to the expression [8]

$$R_{st} = \Gamma g v_g = \Gamma g \frac{c}{n},$$ (1.6)

where v_g is the group velocity of the optical wave, c is the light velocity in vacuum and n is the group refractive index of the material. The confinement factor Γ is introduced to account for the fraction of light within the active layer.

In the laser diode the amplification is caused by injection of charge carriers in the pn-junction. The gain is empirically found to be proportional to the injection current, and can accordingly be linearised with respect to the carrier (electron) density N [12], yielding

$$g = a(N - N_{th}).$$

(1.7)

Here N_{th} is the threshold carrier density and a is the differential gain coefficient.

To describe the wave propagation inside the laser cavity, suppose that the electric field associated with the light is represented by $\wp(t) = E(t)\exp(i\omega t)$. This plane wave can be normalised, so that the absolute square of its amplitude corresponds to the photon number $S(t)$ inside the laser cavity, i.e.

$$S(t) = |\wp(t)|^2 = \wp(t)\wp^*(t),$$

(1.8)

with * denoting the complex conjugate value.

The time derivative of the photon number S is accordingly given by

$$\frac{dS}{dt} = \frac{d(\wp(t)\wp^*(t))}{dt} = \wp(t)\frac{d\wp^*(t)}{dt} + \wp^*(t)\frac{d\wp(T)}{dt}.$$

(1.9)

Since dS/dt is given by Eq. (1.5), dE/dt can be evaluated, yielding the final expression for the field equation

$$\frac{dE(t)}{dt} = \left\{i\omega + \frac{1}{2}\left[\Gamma a(N - N_{th})\frac{n}{c} - \frac{1}{\tau_{ph}}\right]\right\}E(t) + E_{sp}(t),$$

(1.10)

where Eqs. (1.6) and (1.7) have been used. Here ω is the resonant frequency of the diode cavity longitudinal mode, and E_{sp} denote the complex field amplitude due to spontaneously emitted photons. For the sake of simplicity, the spontaneous emission term will be neglected in the following. The relation (1.10) represents the field equation describing the steady-state and the dynamic behaviour of the laser diode.

The loss rate, expressed as the inverse of the photon lifetime, is defined as [12]

$$\frac{1}{\tau_{ph}} = v_g\alpha_t,$$

(1.11)

where v_g is the group velocity and α_t is the total loss coefficient. The total loss is comprised of intrinsic losses α_i and mirror losses α_M, and it is equal to the gain required for the mode to oscillate, i.e. the threshold gain g_{th}. According to Eq. (1.4) it follows that

$$\frac{1}{\tau_{ph}} = v_g(\alpha_i + \alpha_M) = v_g\Gamma g_{th} = \frac{c}{n}\left(\alpha_i + \frac{1}{2L_D}\ln\frac{1}{R_1 R_2}\right).$$

(1.12)

Thus, the losses due to transmission through the two end mirrors are given by

$$\alpha_M = \frac{1}{2L_D}\ln\frac{1}{R_1 R_2}.$$

(1.13)

The optical output power. In order to obtain a relationship between the reflectivities of the diode cavity facets and another measurable physical quantity, an expression for the output power emitted by the laser diode will be derived.

Two of the semiconductor laser parameters which can readily be measured are the light output power P and the injection current I. The variation of the power as a function of the injection current is usually used to characterize the system. Lasing starts at a level of the pumping corresponding to the threshold current $I_{th,s}$ of the solitary diode, and above this point the laser output power is linearly proportional to the injection current.

It is evident that the light output power emanating from both end facets of the laser crystal is proportional to the loss rate due to transmission through these facets. By introducing the totally stored photon energy in a resonator mode, W_{ph}, the output power can consequently be expressed as

$$P = v_g \alpha_M W_{ph}.$$ (1.14)

Under steady-state conditions (d/dt = 0), the photon energy corresponding to the oscillation frequency ω, is given by [12]

$$W_{ph} = \frac{\hbar\omega}{q}\tau_{ph}\left(I - I_{th,s}\right),$$ (1.15)

where $\hbar$ is Planck's constant, τ_{ph} is the photon lifetime, q is the electric charge, I and $I_{th,s}$ are the operating current and the threshold current of the solitary diode, respectively.

Thus, taking Eqs. (1.12), (1.14) and (1.15) into consideration, and introducing an internal efficiency η_i to account for spontaneous emissions and leakage currents [11], we get the following expression for the total output power

$$P = \frac{\hbar\omega}{q}\left(I - I_{th,s}\right)\eta_i \frac{\alpha_M}{\alpha_i + \alpha_M}.$$ (1.16)

In this expression the linearity between the output power and the injection current above threshold is explicit.

Normally one monitors the output power from only one of the facets, e.g. the one corresponding to the reflectivity R_1. The expression for the power P_1 emitted from this facet, can be arrived at by replacing α_M in the numerator in Eq. (1.16) with $\alpha_{M,1} = (1/2L_D)\ln(1/R_1)$. $\alpha_{M,1}$ corresponds to the mirror loss at the relevant facet (compare with Eq. (1.13)), yielding

$$P_1 = \frac{\hbar\omega}{q}\left(I - I_{th,s}\right)\eta_i \frac{(1/2L_D)\ln(1/R_1)}{\alpha_i + (1/2L_D)\ln(1/R_1R_2)}.$$ (1.17)

1.3.2 The laser diode with an external cavity

Light emitted from a laser diode can easily go back into its cavity by an external reflection, because of the low reflectivity of the cavity facets (typically R ≈ 0.32). Thereby, the

dynamic properties of semiconductor lasers are significantly affected by the interference effects between the feedback light and the field inside the diode cavity [13]. If the source laser is not optically isolated from the target, then even a weakly reflecting target has to be considered as part of the lasing system [8].

The effect of optical feedback from an external reflector on the emission spectrum of a semiconductor laser can be explained with a compound cavity model as shown in Fig. 1.3a. The three-mirror resonator is consisting of a Fabry-Perot diode cavity and an external cavity formed by the external reflector (with reflectivity R_3) and the diode facet facing it (with reflectivity R_2).

The resonant mode spacing of the external cavity is determined by the Fabry-Perot cavity condition (compare with Eq. (1.2)), i.e.

$$\Delta\lambda_E = \frac{\lambda^2}{2L_E} \Rightarrow \Delta\omega_E = \frac{\pi c}{L_E},$$

(1.18)

with L_E denoting the external cavity length.

The distribution of resonant modes of the diode cavity and of the external cavity is illustrated in Fig. 1.4. The experiments have been conducted on external cavity lengths L_E considerably larger than the length of the diode cavity L_D, thus the spacing of the external cavity modes is much smaller than that corresponding to the free laser.

Because the laser light has to travel through an additional external cavity, the radiation is reinforced at a wavelength that resonates both in the laser diode cavity and also in the added external cavity. All the other wavelengths, which present larger effective losses, are suppressed. Hence, the external cavity improves the single-mode behaviour of the laser [8]. Semiconductor lasers have a broad gain spectrum half width, and the dominant mode is selected at the combination of modes closest to the gain peak [14].
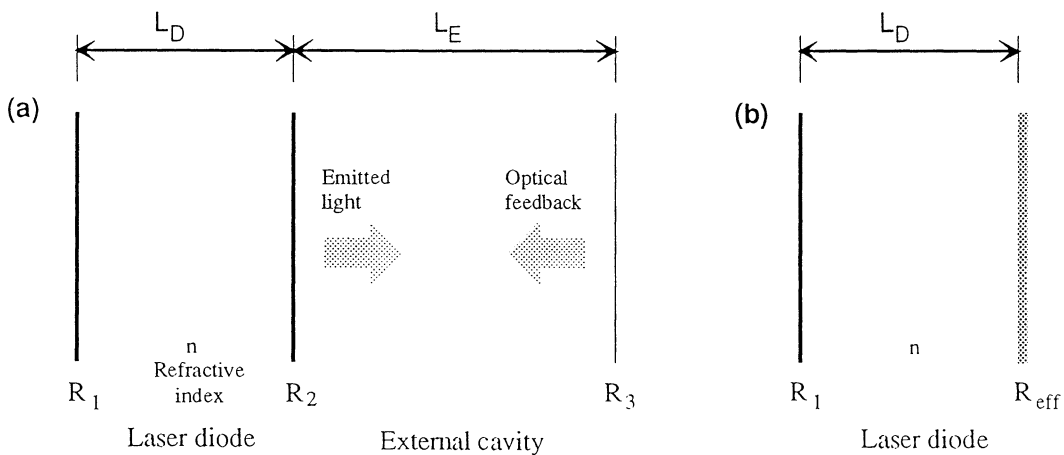
Fig 1.3 A one-dimensional model of the external cavity diode laser: (a) compound cavity built up of the diode cavity and a weak external reflector; (b) equivalent scheme. A typical value for the reflectivity of the uncoated diode facet is $R_1 = R_2 = 32\%$. An external mirror with reflectivity $R_3 = 8\%$ was used in the experiments.
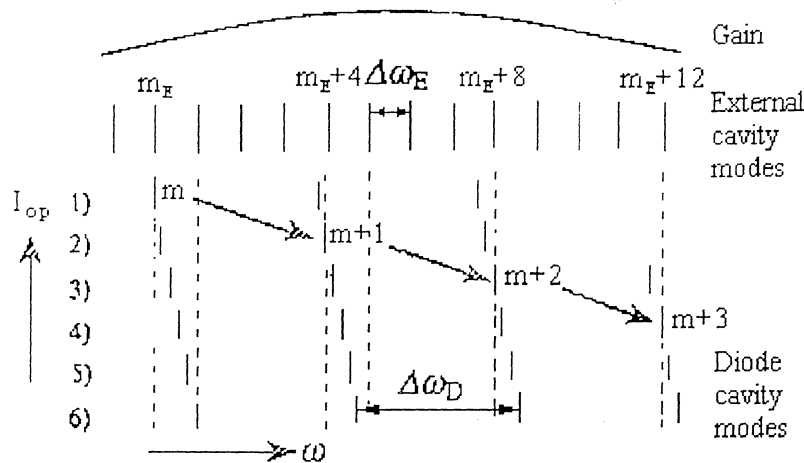
Fig. 1.4 *Mode spacing characteristics of the diode laser cavity and the external cavity.*

When the injection current is increased, the temperature of the semiconductor crystal rises due to dissipated heat, and, at the same time, the refractive index in the active region increases. Crystal temperature variations will additionally lead to a change of diode cavity length and of energy bandgap [11]. All this factors lead to a frequency mismatching at the oscillating mode pair, so that another external cavity mode boosts the power in an adjacent or nearby longitudinal diode laser mode (see Fig. 1.4). This shift of oscillation frequency is known as *mode hopping* [15,16].

The conclusion is that temperature and injection current can be used for selection of the oscillation wavelength, and that careful control of these two parameters is a prerequisite for stable single-mode emission and avoidance of mode hopping.

The field equation. The dynamical properties of a laser diode with an external cavity has been described by Lang and Kobayashi in the form of the following field equation [14]

$$\frac{dE(t)}{dt} = \left\{ i\omega + \frac{1}{2}\left[\Gamma a\left(N - N_{th}\right)\frac{n}{c} - \frac{1}{\tau_{ph}} \right] \right\} E(t) + \kappa E(t - \tau) .$$ (1.19)

Here ω is the longitudinal mode resonant frequency of the solitary diode cavity ($\omega = m\pi c/nL_D$, compare with Eq. (1.1)), and τ is the round-trip time through the external cavity ($\tau = 2L_E/c$). Eq. (1.19) is valid only for *weak* feedback levels of the external reflector, i.e. for single-pass resonance. In our case, the experiments have been done using an external mirror with low reflectivity (<8%). By comparison with Eq. (1.10) we see that the external feedback has been accounted for by adding a single time-delayed term on the right-hand side of the equation.

For the derivation of this expression, we consider an equivalent model of the compound cavity system as illustrated in Fig. 1.3b. An *effective mirror reflectivity* R_{eff} is introduced, accounting for the reflected radiation from the inner laser facet facing the external cavity and from the external mirror, as well as for the phase delay of the external feedback [17,18]. We take into consideration even the optical losses due to transmission and coupling back into the diode cavity, by introducing a coupling efficiency η [17,19,20] and an external reflectivity R_{ext} so that

$$R_{ext} = \eta R_3 .$$ (1.20)

Assuming a stationary field $E_i \exp(i\Omega t)$ incident from the left on the inner facet (Ω denotes the oscillating frequency of the compound cavity laser), the total reflected field at this facet is

$$E_r e^{i\Omega t} = \left[\sqrt{R_2} + (1 - R_2)\sqrt{R_{ext}}\, e^{-i\Omega\tau} + (1 - R_2)R_{ext}\sqrt{R_2}\, e^{-i2\Omega\tau} + ...\right] E_i e^{i\Omega t}. \qquad (1.21)$$

An effective amplitude reflectivity r_{eff} can then be defined as the ratio E_r/E_i. If multiple reflections in the external cavity are neglected, the effective reflectivity is found to be

$$\sqrt{R_{eff}} = r_{eff} = \sqrt{R_2}\left[1 + (1 - R_2)\sqrt{\frac{R_{ext}}{R_2}}\, e^{-i\Omega\tau}\right] = \sqrt{R_2}\left(1 + ae^{-i\Omega\tau}\right), \qquad (1.22)$$

where parameter a is introduced as

$$a = (1 - R_2)\sqrt{\frac{R_{ext}}{R_2}} = (1 - R_2)\sqrt{\frac{\eta R_3}{R_2}}. \qquad (1.23)$$

The total loss rate of the compound cavity, $1/\tau_{ph,e}$, can be computed using the result derived for the threshold condition for the solitary diode (see Eq. (1.12)). We apply it on the equivalent scheme of the external cavity configuration shown in Fig. 1.3b, by replacing R_2 in the expression for the mirror losses with the new effective reflectivity R_{eff}. We then obtain

$$\frac{1}{\tau_{ph,e}} = \frac{c}{n}\left(\alpha_i + \frac{1}{2L_D}\ln\frac{1}{R_1 R_{eff}}\right) = \frac{c}{n}\left[\alpha_i + \frac{1}{2L_D}\ln\frac{1}{R_1 R_2} - \frac{1}{L_D}\ln\left(1 + ae^{-i\Omega\tau}\right)\right]. \qquad (1.24)$$

The first two terms on the right-hand side represent the loss rate of the solitary diode laser (compare with Eq. (1.12)). Assuming $a \ll 1$, i.e. low feedback $\eta R_3 \ll R_2$, the following relationship for the total loss of the compound cavity holds approximately

$$\frac{1}{\tau_{ph,e}} = \frac{1}{\tau_{ph}} - \frac{ca}{nL_D}e^{-i\Omega\tau}. \qquad (1.25)$$

By inserting this expression in the field equation (1.10) for the laser diode, Eq. (1.19) is arrived at. The feedback strength κ is then given by

$$\kappa = \frac{ca}{2nL_D} = \frac{a}{\tau_c}, \qquad (1.26)$$

where τ_c is the round-trip time for the light in the diode cavity.

The optical output power. We now use the same approach as in Sect. 1.3.1 to obtain an expression for the light output power emitted from the back laser facet, corresponding to the reflectivity R_1. Considering the model in Fig. 1.3b, we replace R_2 in the Eq. (1.17) with

the effective reflectivity R_{eff} (given by Eq (1.22)), and find the output power from the back facet given by

$$P_{1,e} = \frac{\hbar\Omega}{q}\left(I - I_{th,e}\right)\eta_i \, \frac{(1/2L_D)\ln(1/R_1)}{\alpha_i + (1/2L_D)\ln(1/R_1 R_{eff})} \, .$$

(1.27)

Here Ω is the oscillating frequency of the external cavity laser, and $I_{th,e}$ is the threshold current for the compound cavity. Thus, from the above expression it can be seen that the optical output power is a function of the effective reflectivity.

1.4 Light scattering by particles and Fraunhofer diffraction

Scattering processes in the atmosphere form the basis of well known phenomena, often taken for granted, such as the blue of the clear sky, the red of the sunset glow, and the "miraculous" appearance of the rainbow after a heavy shower [3].

This section gives a very brief and limited background to the phenomenon of light scattering by particles. A more extensive and detailed presentation of this subject can be found for instance in the book by van de Hulst [21]. Further, a short presentation of Fraunhofer diffraction by a slit is also given.

A parallel electromagnetic beam illuminating a particle will be attenuated due to absorption and scattering by the particle. This attenuation of light is called extinction, and it can consequently be written as

Extinction = Scattering + Absorption.

A small particle will scatter an incident electromagnetic wave in different directions. This is due to emission of radiation from the electric charges in the particle, which have been accelerated by the electric field. The scattering is called *elastic* if the incident and scattered radiation have the same frequency, or *inelastic* if the wavelength is altered.

Let a particle with a size d (corresponding for instance to the diameter of a spherical particle), made up of a material with a complex refractive index m, be illuminated by a plane, monochromatic wave of wavelength λ. A *dimensionless size parameter* α is usually introduced, connecting the particle's size d and the wavelength λ through the relation

$$\alpha = \frac{\pi d}{\lambda} \, .$$

(1.28)

The spatial distribution of the light scattered by the particle per unit solid angle can be described by a *dimensionless scattering function* Q_s that depends on the scattering angle θ, the size parameter α, and the refractive index m of the material.

At any point in the distant field, the scattered electromagnetic radiation has the character of a spherical wave, in which energy flows outward from the particle. The intensity of the scattered light (defined as energy flux per unit area) in a point at a distance r from the particle and corresponding to a scattering angle θ can consequently be written as

$$I_s(\theta, r) = \frac{Q_s(\theta, \alpha, m)}{k^2 r^2} I_0 .$$

(1.29)

Here k represents the wave number (k = $2\pi/\lambda$), and I_0 is the illumination intensity.

Further, a *scattering cross-section* C_s is usually introduced, defined as the quotient between the power of the scattered light and the intensity of the incident light, i.e.

$$C_s = \frac{P_s}{I_0} .$$

(1.30)

Consequently, the scattering intensity can also be written as

$$I_s = \frac{1}{r^2} C_s I_0 ,$$

(1.31)

while the scattered electric field is then given by

$$E_s = \frac{1}{r} \sqrt{C_s} E_0 e^{-ikr} ,$$

(1.32)

where E_0 is the amplitude of the incident light.

The energy absorbed inside the particle may by definition be put equal to the energy incident on the area C_a, called *absorption cross-section*, so that the total energy removed from the original beam corresponds to the so-called *extinction cross-section* C_e, defined as

$$C_e = C_s + C_a .$$

(1.33)

It can be shown that for large particles, the extinction cross-section is equal to the double of the geometrical cross-section of the particle [21]. It may seem as a paradox, that a particle can remove from the incident beam twice the amount of light it intercepts. However, this is a consequence of the boundary condition which demands that the electromagnetic field must be continuous at the particle surface. In fact *all* scattered light, including that at small angles, is counted as removed from the beam.
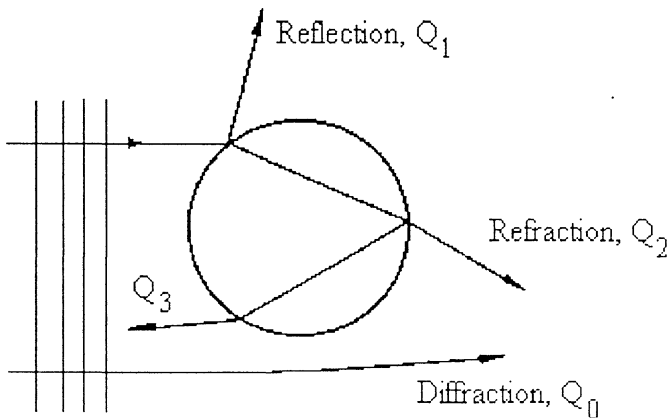
Fig. 1.5 *Decomposition of scattered light in components according to ray optics.*

There are two limiting cases for the phenomenon of elastic light scattering by small particles [4,21]. The scattering of light from particles that are much smaller than the wavelength of light, i.e. $\alpha \ll 1$, is called *Rayleigh* (or *dipole*) *scattering*. If the particles instead are comparable or greater in size than the wavelength of the impinging light one speaks of *Mie scattering*.

While the scattered light is homogeneously and symmetrically distributed in the case of Rayleigh scattering, the Mie scattering is characterized by intensity oscillations in the scattering directions.

Another important feature of the scattered light intensity is its strong particle size dependence. The intensity for Rayleigh scattering is proportional to the sixth power of the particle diameter ($I \propto d^6$). For Mie scattering, the scattered light intensity is proportional to the particle's projected area ($I \propto d^2$).

Lorenz-Mie scattering. Gustav Mie has 1908 presented an analytical method for derivation of the intensity distribution of the light scattered by spherical particles illuminated by a plane wave [22]. His method was based on the so-called Lorenz-Mie scattering theory, which provides an exact solution to Maxwell's equation of electromagnetic propagation. (Lorenz has earlier independently derived corresponding expressions [23].)

Nevertheless, the results of Lorenz-Mie theory are very complex and geometrical optics can be employed as good approximations for particles very large compared with the wavelength of light ($\alpha \gg 1$) [21]. In this case it is possible to distinguish rays hitting various parts of the particle's surface. The rays hitting the particle and passing along it give rise to scattering due to three distinct phenomena: diffraction, reflection, and refraction (see Fig. 1.5). The scattering function Q_s can be expressed as the sum of these three components, according to

$$Q_s(\theta, \alpha, m) = Q_0(\theta, \alpha) + Q_1(\theta, m) + Q_2(\theta, m) .$$
(1.34)

Q_0 is the diffracted part of scattered light. Its angular distribution depends on the size parameter α, but is independent of the optical properties of the particle, i.e. the refractive index of the material. Q_1 and Q_2 are the components scattered by reflection on the surface of the particle and by two consecutive refractions by the surface, respectively. Their angular distribution is independent of the size parameter, but is influenced by the optical constants of the material and also by the shape of the particle.
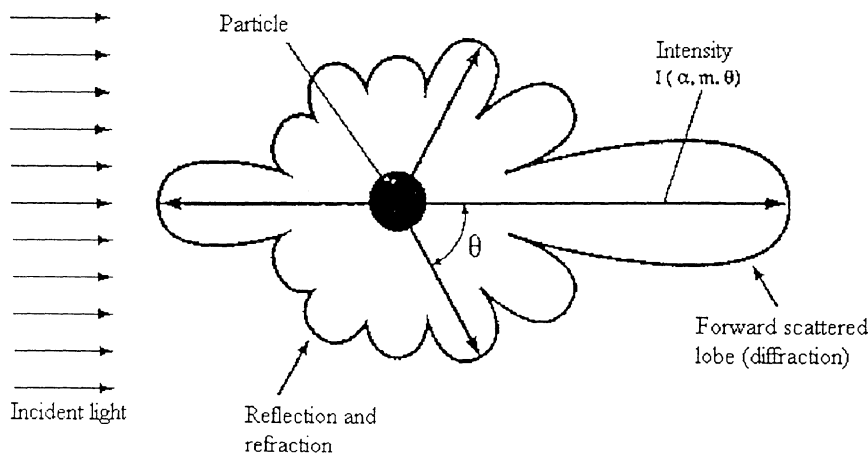

Fig. 1.6 *Single particle light scattering.*

The diffraction component Q_0 of the scattered light is compressed into a narrow but very intense forward lobe, as illustrated in Fig. 1.6. It dominates strongly over the other components (and can actually be several orders of magnitude larger).

For low scattering angles ($\theta < 10°$), and for particle dimensions $d > 4\text{-}5\lambda$, the diffraction part of scattered light can be approximated by Fraunhofer diffraction [2,24].

The conclusion is that the scattered light should be collected in the *near-forward direction*, where the diffraction part (proportional to the particle size) dominates and where the influence of the optical properties of the particle is minimised. In this regime one can approximate the scattered light distribution by the Fraunhofer diffraction [25].

Fraunhofer diffraction. A characteristic of Fraunhofer diffraction is that the angular distribution of scattered light intensity is determined by the particle's shape, and is inversely proportional to the size of the particle.

The condition for Fraunhofer diffraction is that the plane of observation is situated in the so-called *far-field region*, i.e. is very distant. This practically means that the distance R from the diffracting object to the plane of observation must satisfy the condition

$$R >> \frac{d^2}{\lambda},$$
(1.35)

where d is the dimension of the diffracting object and λ is the wavelength of light.

Here we shall present the expressions for Fraunhofer diffraction by a slit [26], which will be employed in the evaluation of the experimental findings in Sect 3.1.

The light intensity distribution resulting from diffraction of a coherent plane wave by a single slit of width d, is given in the Fraunhofer approximation by

$$I(\theta) = I(0)(\frac{\sin \beta}{\beta})^2,$$
(1.36)

where β is defined as

$$\beta = \frac{kd}{2}\sin \theta.$$
(1.37)

Here θ is the scattering angle, I(0) is the intensity at the principal maximum, and k is the propagation number ($k=2\pi/\lambda$).

The extrema of $I(\theta)$ occur at values of β for which $dI/d\beta$ equals zero, that is

$$\frac{dI}{d\beta} = I(0)\frac{2\sin \beta(\beta\cos\beta - \sin \beta)}{\beta^3} = 0.$$
(1.38)

Hence, the intensity distribution has minima, equal to zero, when $\sin\beta = 0$, whereupon $\beta = \pm\pi, \pm 2\pi, \pm 3\pi, ...$ According to Eq. (1.37), it follows that the zeros of irradiance will occur when

$$d \sin \theta_m = m\lambda , \qquad (1.39)$$

where m is a whole number $m = \pm 1, \pm 2, \pm 3, ...,$ and θ_m is the scattering angle corresponding to the m-th irradiance minimum.

The maxima of irradiance correspond to the solution of the transcendental equation $\tan \beta = \beta$. The derived numerical solutions of this equation are presented in Table 1.1.

Table 1.1 *Numerical solutions of the equation tanβ = β, and corresponding order of the subsidiary intensity maximum in the Fraunhofer diffraction pattern.*

| β							
	$\pm 1.430\pi$	$\pm 2.459\pi$	$\pm 3.471\pi$	$\pm 4.477\pi$	$\pm 5.482\pi$	$\pm 6.484\pi$	$\pm 7.487\pi$
Order of the maximum	1st	2nd	3rd	4th	5th	6th	7th

The experimental evaluation of the aerosol particle sensor was conducted on fibres (see Chaps 2 and 3). In order to show the relevance of the presented expressions for the Fraunhofer diffraction, valid for scattering by a slit, we shall consider the following experiment:

Given an aperture and an obstacle, shaped so that the transparent and the opaque regions on the two objects are complementary, let E_1 and E_2 be the electromagnetic field amplitudes arriving at a distant point of observation when either the two objects, respectively, is in place. The *Babinet's principle* states that in the far-field region, i.e. at a distant point of observation, the two electromagnetic fields are precisely equal in magnitude and 180° out of phase, i.e. $E_1 = -E_2$ [21,26]. Thus, the same light intensity distribution, defined as $I = <E^2>$, will be generated with either the aperture or the obstacle in place. Consequently, the results obtained for the distribution of diffracted light intensity generated by a slit can also be applied for a fibre of same thickness.

1.5 A theoretical model for the light-particle interaction in the external cavity of a laser diode

In the following a theoretical model for the particle interaction with the electromagnetic wave in the external cavity of the laser system will be discussed. An expression for the effect of this disturbance on the light output power will also be given.

By analogy with the method used to describe the two resonator cavity system in Sect. 1.3.2 (see Fig. 1.3), we adopt a one-dimensional model for the *disturbed* compound cavity. The reflectivities of the inner laser facet and the external mirror, as well as the influence of the scattering and absorption due to the particle inside the passive external cavity are all accounted for by a total effective reflectivity $R_{eff,p}$ (see Fig. 1.7b,c).
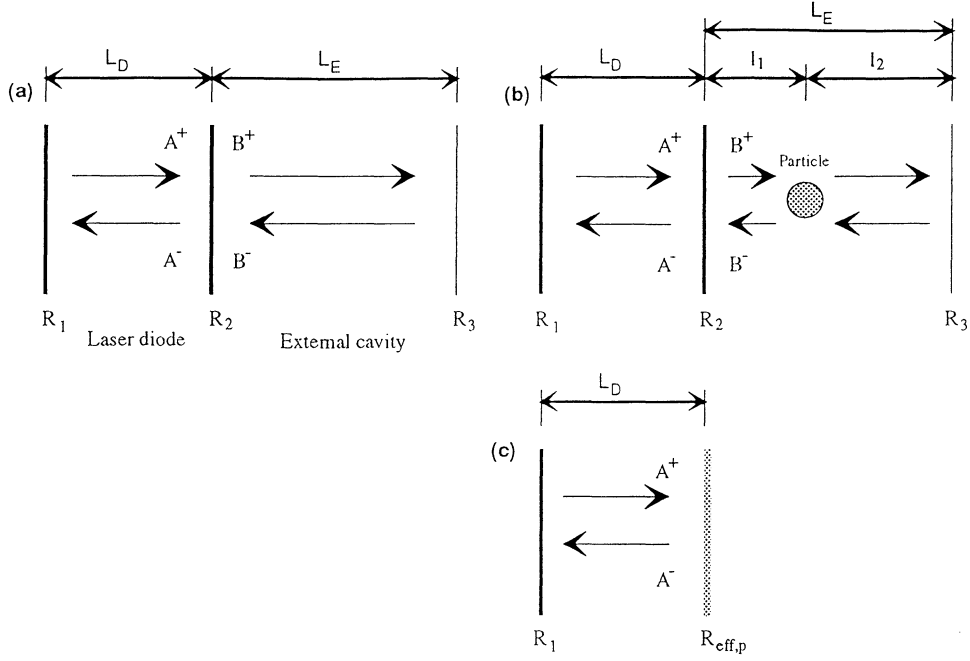
Fig. 1.7 *Electromagnetic waves in a laser diode coupled to an external cavity: (a) without external disturbance; (b) with a small particle inside the external cavity; (c) equivalent scheme for the system with a small particle.*

The effect of the disturbance caused by an aerosol particle can be measured as a variation of the light output power emitted from one of the diode facets. Similarly to Eq. (1.27), we obtain the output power emitted from the back diode facet (at the left in Fig. 1.7)

$$P_{1,p} = \frac{\hbar\Omega}{q}\left(I - I_{th,e}\right)\eta_i \, \frac{(1/2L_D)\ln(1/R_1)}{\alpha_i + (1/2L_D)\ln(1/R_1 R_{eff,p})} . \tag{1.40}$$

Here we have assumed that the oscillating frequency Ω and the threshold current $I_{th,e}$ for the compound cavity system will remain unchanged. This should be a plausible assumption, because the variation is initiated by a *small* disturbance of the feedback radiation. Comparing Eq. (1.27) with Eq. (1.40) we see that if the effective reflectivity including particle disturbance $R_{eff,p}$ is smaller than the effective reflectivity of the undisturbed compound system R_{eff}, then the output power emitted from the back facet will decrease $P_{1,p} < P_{1,e}$.

In order to obtain an analytical expression for the total effective reflectivity of the front (right) facet of the laser $R_{eff,p}$, the boundary-value problem at this facet for the fields in the compound cavity must be solved [14,19,27].

In the following derivation only single reflections are taken into consideration, which is a valid approximation for low feedback conditions. We consider the system in steady-state conditions and regard the particle located statically inside the beam. (This does not constitute a strong restriction on the movement of the particle, since the time factor of a laser diode is extremely short — in the order of nanoseconds [28].)

Further, it is assumed that essentially only the forward and the backscattered light from the particle will be effectively coupled back into the laser diode cavity, and will thus influence

the lasing system. Since all reflecting surfaces (including the external mirror) are plane, there is a strong sensitivity of the feedback coupling efficiency to the reflectance angle. Thus, light scattered in other directions is presumably not coupled back. (Compare also with the critical dependence of feedback coupling on the tilt of the external mirror, discussed in Sect 2.1.2).

We consider the model illustrated in Fig. 1.7b, where the electric waves in the two cavities are decomposed into right and left travelling waves. At the inner boundary

$$A = A^+ + A^-$$
$$B = B^+ + B^-.$$

(1.41)

Here the time dependence of the complex optical field, given as $\exp(i\Omega t)$, has been omitted. We introduce amplitude reflectivities and an amplitude transmission defined as

$$r_2 = \sqrt{R_2}$$
$$r_{ext} = \sqrt{R_{ext}} = \sqrt{\eta R_3}$$
$$t = \sqrt{1 - R_2}$$

(1.42)

We also denote the square roots of forward scattering and backscattering cross-sections by

$$\sqrt{C_s(\theta = 0)} = c_0$$
$$\sqrt{C_s(\theta = \pi)} = c_\pi,$$

(1.43)

respectively.

The electric field must be continuous at the considered boundary, yielding the following set of equations

$$A^- = A^+ r_2 + B^- t$$
$$B^+ = A^+ t$$
$$B^- = B^+ r_{ext} \sqrt{1 - \frac{C_e}{S}} e^{-i2kL_E} + \frac{1}{2l_1 l_2} B^+ r_{ext} c_0^{\ 2} e^{-i2kL_E} + \frac{1}{l_1} B^+ c_\pi e^{-i2kl_1}.$$

(1.44)

The distances L_E, l_1 and l_2 are indicated in Fig.1.7b, while k denote the propagation number ($k = 2\pi/\lambda$). As for the scattering and absorption by the particle, the expressions in Sect. 1.4 have been employed (see Eq. (1.32)). The factor $\sqrt{1 - C_e / S}$ in the expression for B^- represent the transmitted light beyond the particle. C_e is the extinction cross-section of the particle due to scattering and absorption ($C_e = C_s + C_a$), and S denote the geometrical cross-section of the laser beam.

From the set of equations (1.44) we get

$$A^- = A^+ r_2 \left\{ 1 + t^2 \frac{r_{ext}}{r_2} \left[\left(\sqrt{1 - \frac{C_e}{S}} + \frac{c_0^{\ 2}}{2l_1 l_2} \right) e^{-i2kL_E} + \frac{1}{r_{ext}} \frac{c_\pi}{l_1} e^{-i2kl_1} \right] \right\}.$$

(1.45)

The effective amplitude reflectivity for the front facet including the particle disturbance is consequently given by

$$\sqrt{R_{eff,p}} = r_{eff,p} = \frac{A^-}{A^+} = \sqrt{R_2}\left[1 + (1 - R_2)\sqrt{\frac{R_{ext}}{R_2}}\left(\sqrt{1 - \frac{C_e}{S}} + \frac{c_0^2}{2l_1l_2} + \frac{1}{\sqrt{R_{ext}}}\frac{C_\pi}{l_1}e^{i2kl_2}\right)e^{-i2kL_E}\right].$$

(1.46)

This expression should be compared with the one in Eq. (1.22), corresponding to the effective amplitude reflectivity of the same facet but without any particle disturbance. (Consider also the phase due to the time delay $\exp(-i\Omega\tau) = \exp(-i2kL_E)$). Hence, the difference in amplitude reflectivity δ due to the disturbance can be written as

$$\delta = r_{eff} - r_{eff,p} = (1 - R_2)\sqrt{\eta R_3}\left(1 - \sqrt{1 - \frac{C_e}{S}} - \frac{C_s(\theta = 0)}{2l_1l_2} - \frac{1}{\sqrt{\eta R_3}}\frac{\sqrt{C_s(\theta = \pi)}}{l_1}e^{i2kl_2}\right)e^{-i2kL_E}$$

(1.47)

This theoretical result may be used to explain some of the basic features of the experimental findings described in Chapter 3 and 4 of this thesis.

It can be seen from this equation that if the particle is removed, i.e. $C_s = C_e = 0$, then, as expected, δ will be equal to zero. The sensitivity to particle disturbance will increase, i.e. the variation of the optical output power (defined as the measured signal) will be large, if the laser beam cross-section S or the reflectivity R_2 are made small. The distance l_1 from the particle to the front facet of the laser diode affects primarily the level of influence of the backscattering by the particle. The dominating term due to the light-particle interaction is the one corresponding to light extinction $\sqrt{1 - C_e / S}$.

As the laser light strikes the particle, the light scattered in the forward direction (corresponding to $C_s(\theta = 0)$) mainly due to diffraction, will be much stronger than the backscattered light (corresponding to $C_s(\theta = \pi)$) caused by reflection (compare with Sect. 1.4). Because the optical feedback from the external mirror is low, the subsequent scatterings by the particle of back-coupled light are negligible. This implies that the forward scattering should also have a greater effect on the interaction between the particle and the lasing system.

1.6 Aerosols and aerosol measurement

This section briefly discusses the sources and the physical properties of aerosol particles, as well as the effects on the human health. Some aerosol measurement fundamentals are also mentioned.

The term *aerosol* (also called *particulate matter*) refers to an assembly of liquid or solid particles suspended in a gaseous medium [29]. The air around us can, thus, be seen as an aerosol. The atmosphere consists of a complex and dynamic mixture of gases, vapour, and aerosol particles. The particles are generated both by natural sources and by human activity.

Natural processes generating aerosol particles include volcanic eruptions, sea-spray and forest fires (in the last case minute oil droplets are arising from the distillation of wood). There are also biological particles such as fungi, pollens (see magnification on the front page of this thesis), and viruses.

As for the man-made aerosol particles, they originate for instance from combustion processes (e.g. car exhaust fumes, agricultural burning, and tobacco smoke) and industrial emissions. In the indoor environment, walls, floors, and ceilings may release glass fibres, asbestos fibres, and mineral wool. Clothing articles are also sources of natural and synthetic organic fibres.

The aerosol particles may have a great diversity in size, shape, density, and chemical composition. The range of particle sizes extends over five decades from about 0.001 µm to about 100 µm [4,29]. The size of an aerosol particle is important for the study of transportation and deposition. Most real aerosol systems consist of particles of irregular shape [2].

In work environments, the particle mass concentration typically ranges from about 0.1 mg/m^3 to about 10 mg/m^3, while in ambient and indoor air it is usually less than 0.1 mg/m^3 [2]. Due to very low concentrations, particulate pollution monitoring in the atmosphere requires aerosol detectors of high sensitivity.

The health effects of aerosols inhaled in the nose and in the mouth depend on the concentration and the site of deposition within the respiratory system. Particle size is the most important factor affecting the location of deposition [29]. For example, fibres must be smaller than about 2-3 µm diameter to reach the thoracic region and thinner still to reach the air exchange regions of the respiratory system [2]. Hazardous aerosol particles have been associated with several diseases, such as allergy, asthma, asbestosis, and lung cancer.

Particle size and shape can be quite complex, and the experimentally obtained values depend on the measurement technique. A commonly used term in aerosol particle measurement is that of *equivalent diameter*. An equivalent diameter is defined as the diameter of a sphere having the same value of a specific physical property as the irregularly shaped particle being measured [29]. The equivalent particle size may for example be based on the light scattering properties of the particle under consideration. The particle size indicated by an optical particle counter must in fact be regarded as an optical equivalent particle size.

By development of an aerosol sensor, one must first identify the particle properties that need to be measured and the conditions under which the measurement must be made. Each aerosol measurement technique covers a unique range of particle concentrations, sizes, and shapes determined by the limitation of the measuring instrument [2].

2. Design of an optical sensor and experimental measurements on fibres

2.1 The experimental set-up

This section describes the experimental arrangement used for the measurements. Fig. 2.1 gives a schematic representation of the laser diode coupled to an external cavity, the imaging optics, and the monitoring instruments.

The working principle of the sensor is that it sizes and counts individual airborne particles as they pass through an illuminated volume located in the external cavity of a diode laser. As the particles pass through this region, they scatter light. This light is collected over a solid angle by the receiving optics and is then imaged onto a CCD camera.

The experimental arrangement used is shown in Fig. 2.2. It is easy to construct and uses mainly inexpensive components.

In the following, we shall start with a short description of the light source, then continue by extending it with an external cavity. The imaging optics used to collect the near-forward scattering light are subsequently described and, finally, the detection instruments are presented.

2.1.1 The laser system

Most optical particle-sizing techniques use coherent laser light because of its intensity, monochromaticity, and coherence [2]. Semiconductor lasers are extremely robust, user-friendly, and highly efficient solid state lasers (see depiction in Fig. 2.3a).

Tests have been performed on a number of different laser diodes (se Appendix A). Finally, a single-mode GaAs-AlGaAs double heterostructure laser (Sony SLD114VS) emitting light in the near-infrared region was chosen. The specifications for this component are given in Table 2.1.

Table 2.1 *Laser diode specifications (T = 20.75 °C).*

Device	Structure	I_{th} (mA)	λ (nm)	Divergence angle (deg.) $\theta_\perp$	$\theta_\parallel$	Astigmatism (μm)
Sony SLD114VS	index guided, AlGaAs, double hetero-structure	19.4	781.84	30	10	5

Although the emitted light is still in the wavelength range for human vision, said to be roughly 390 nm to 780 nm [26], it was necessary to use an infrared display-card to visualise the beam due to the low output intensity employed.

Real-time
spectrum

$\lambda = 781.8$ nm

Data acquisition PC

Computer

Oscilloscope

CCD Camera &
Beamprofiler

Low-pass filter

Trigger signal

Discriminator

ND-Filter

Lens L3

Lens L2

I_{mon}

Diode laser
driver

CCD
Camera

I_{op} I_{mon}

Scattered light

Dump spot

Collecting lens L1

Shielding

Particle

Entrance slit

Jobin-Yvon
spectrometer

Lens

Lens Beam splitter
R= 50%

Collimating lens
NA= 0.55

LD PD
Sony
SLD114VS

Mirror R= 8%

External cavity

Fig. 2.1 *The experimental set-up. The Sony laser diode is operated at a current $I_{op} = 18.9$ mA and it is temperature controlled at $T = 20.75$ °C. The external cavity length is $L_E = 75$ mm.*

Fig. 2.2 *The experimental arrangement: (a) the external cavity and the Fourier transform lens; (b) view of the diode laboratory.*

(a)

(b)
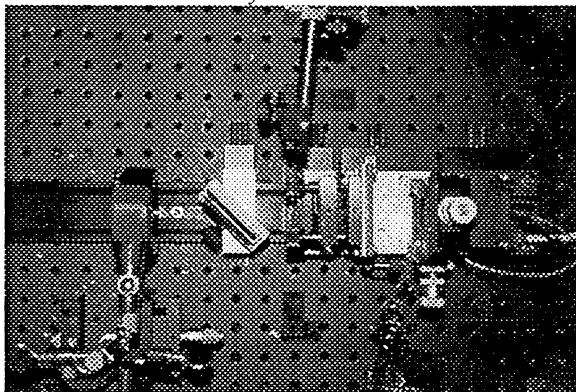
(a) **(b)**

Fig. 2.3 *The laser diode: (a) component structure; (b) optical characteristics.*

The reflection of radiation at the uncoated end facets of the semiconductor crystal occurs because of the mismatch between the refractive index of the semiconduct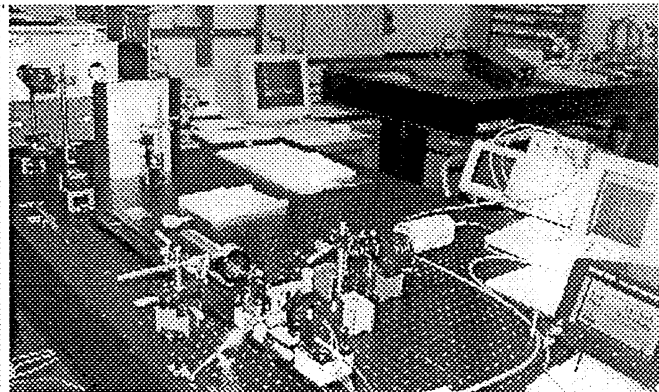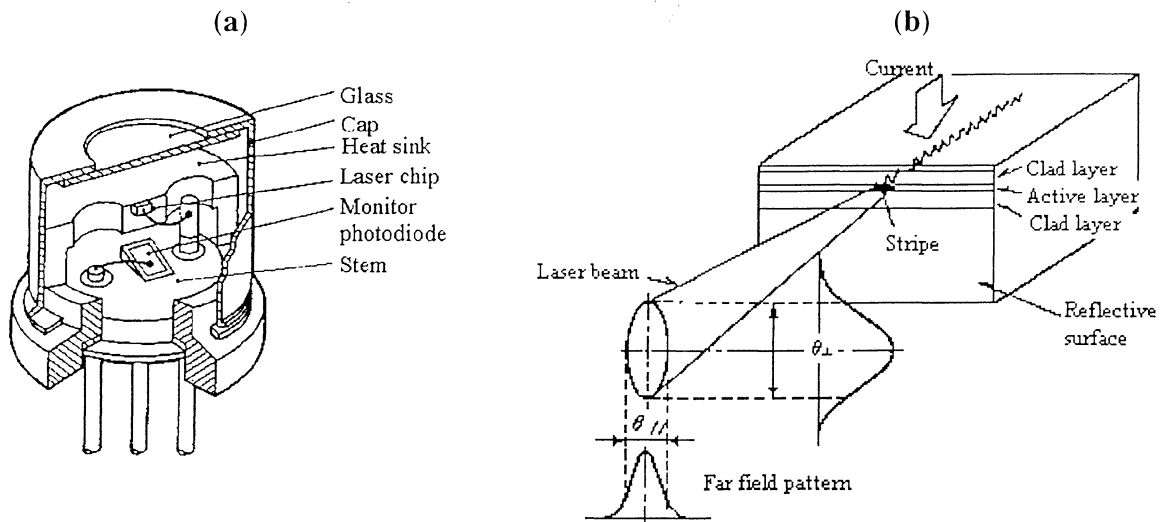or material (n ≈ 3.6) and that of the surrounding air. According to Fresnel's equation [26], the reflectivity at normal incidence is given by

$$R = \left(\frac{n-1}{n+1}\right)^2 \approx 0.32 .$$

(2.1)

The divergence of the emitted beam is a consequence of the unavoidable influence of diffraction, while the asymmetry of the divergence angle (compare with Table 2.1) is caused by the different dimensions of the active region in the lateral and vertical direction (see Fig. 2.3b).

A moulded glass aspherical lens (Geltech 350230) is used to collimate the divergent laser beam. In order to avoid unwanted reflections, the surfaces of this multi-element lens are AR-coated at 600-1050 nm.

The lens has a numerical aperture NA = 0.55. The numerical aperture is defined as $NA = n_0 \sin\theta_{max}$, where n_0 is the refractive index of the immersing medium (air), and θ_{max} is the half-angle range of the maximum cone of light picked up by the lens [30]. The maximum acceptance angle corresponding to the given numerical aperture of the collimating lens is $\theta_{max} \approx 33°$. This angle is larger than the divergence angle of the laser diode, which means that the emitted laser light will readily be transmitted through the lens.

The collimating lens holder is provided with transversal and longitudinal adjustments in order to facilitate the lens alignment. The position of the lens was optimised in order to obtain the lowest possible divergence.

For diagnostic purposes, a laser beam analyzer was used to characterize the light beam. The Geltech collimator produced a highly symmetrical beam profile, without serious wavefront distortions. The vertical and the horizontal dimensions of the elliptical cross-section of the beam were found to be 4 mm and 1.7 mm, respectively. The light intensity profile is approximately a Gaussian one (see Fig 2.4). Additionally, interference fringes are clearly
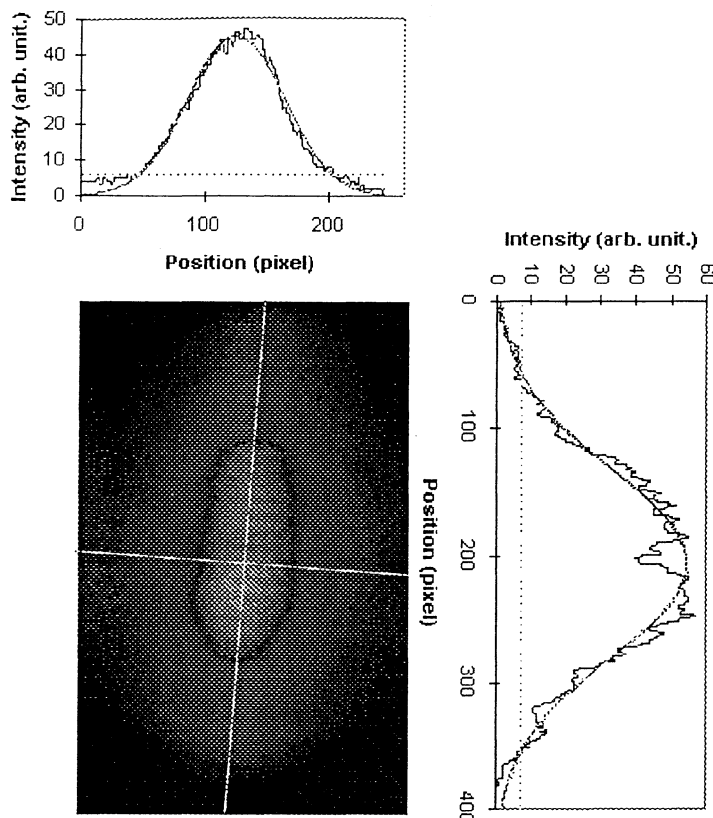
Fig. 2.4 *Recorded output beam profile for the collimated solitary laser beam. The intensity distributions in the horisontal respectively vertical directions, along centered cross-sections, are shown beside the image. The path of the cross-sections are indicated by the bright cross. For comparison, gaussian functions are fitted to the experimental intensity distributions (dashed line). The dotted line indicate the extent of the $1/e^2$ beam radius.*

discernible, possibly caused by fed-back light from the collimator lens surfaces [31], or by reflections from the ND filter in front of the beam analyzer. (The laser was emitting excellent single-frequency radiation, which also implies TEM_{00} mode operation, so it is not possible that the intensity modulation is associated with higher order spatial modes.)

The emitted light spectrum was detected with a Jobin-Yvon spectrometer (of Czerny-Turner type) as depicted in Fig. 2.1. A lens was used to focus the laser light on the entrance slit, so as to fill the diffraction grating inside the spectrometer. The resolving power $\mathfrak{R}$ of the grating spectrometer is determined by the total number of illuminated lines N and by the diffraction order m, i.e.

$$\mathfrak{R} = \frac{\lambda}{\delta\lambda} = N \cdot m,$$

(2.2)

where $\delta\lambda$ is the resulting linewidth of the spectrometer when using monochromatic light of wavelength λ [3]. Thus, underfilling would diminish the resolving power of the spectrometer. The slit width and the lens position were optimised in order to increase the transmission of laser light into the spectrometer and to minimise the linewidth of the spectral lines.

A CCD camera placed at the exit plane of the spectrometer was used to record the real-time spectrum. The dark current caused by the thermally released electrons [30], was reduced by cooling to -10 °C. By acquisition of the optical spectra, the CCD integration time ranged between 0.01 and 10 seconds. After the CCD chip was red off, data was sent to a computer for analysis.
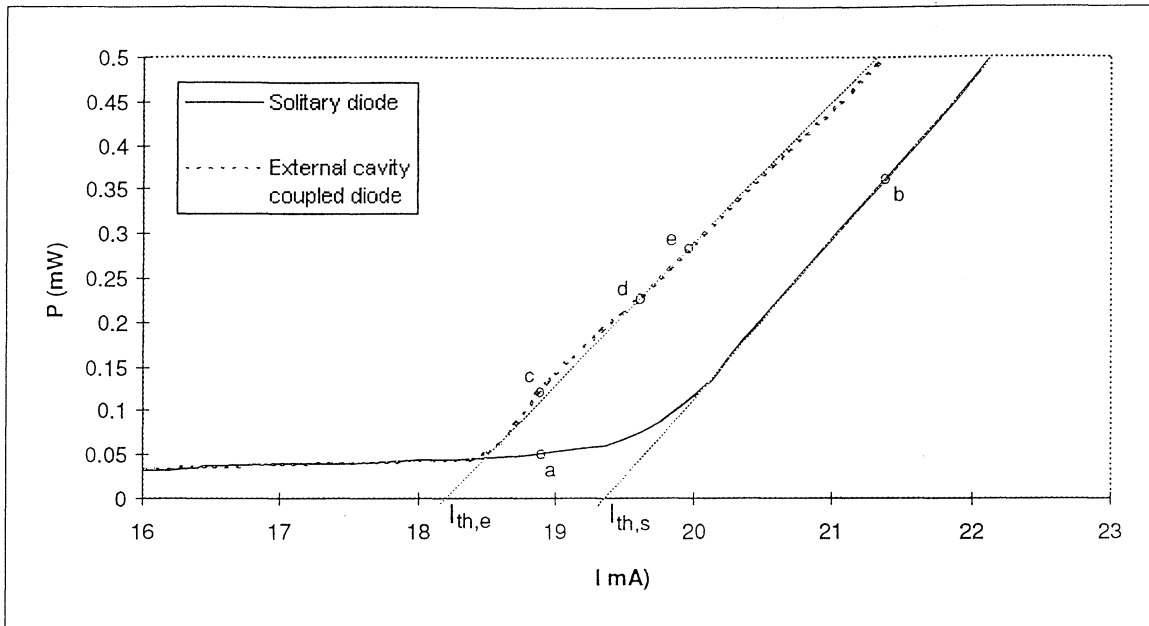
Fig 2.5 *Optical output power versus forward current for the laser diode at the temperature T = 20.75 °C. The solid line corresponds to the solitary diode characteristic, and the dashed line to the external cavity coupled system characteristic. The gray dotted lines are fitted asymptotes, used for evaluation of the threshold currents. The indicated operating points at injection currents I_{op} = 18.9 mA (a) and (c), I_{op} =19.6 mA (d), I_{op} =20.0 mA (e), and I_{op} =21.4 mA (b), respectively, correspond to emitted wavelength spectra presented in Fig. 2.6.*

The wavelength scale was calibrated using the lines from an argon lamp [32].

The injection current and the temperature of the laser diode were both controlled via an integrated diode laser driver (Melles Griot 06DLD103).

The laser was powered with low-noise dc current, and the injection current was controlled with a sensitivity of 0.1 mA.

In order to avoid "mode hopping" (compare with Sect. 1.3.2) caused by surrounding temperature variations, the temperature of the semiconductor crystal was stabilised by a Peltier element. This thermoelectric cooler, driven by a servomechanism, was placed between the laser mount and the baseplate.

A basic feature of a laser diode is its *output power-current (P-I) characteristic* as shown in Fig. 2.5. The threshold current of the solitary laser diode $I_{th,s}$ is defined as the intersection point between the asymptote and the current axis. It marks the transition from predominantly spontaneous to stimulated generation of photons. The threshold current increases with rises in temperature. This dependence is usually empirically described by the relation $I_{th} \propto \exp(T/T_0)$, with a characteristic temperature T_0 [10]. From the plot shown in Fig. 2.5 (solid line) it has been evaluated that at the temperature T = 20.75 °C the threshold current for the solitary diode was $I_{th,s}$ = 19.4 mA.

The optical spectra corresponding to the operating points (a) and (b) marked in Fig. 2.5 are shown in Fig. 2.6a,b, respectively. The emission lines belong to the longitudinal modes of the diode cavity. Possible external cavity modes, separated a few picometer apart, could not be resolved since the spectrometer resolution was limited to approximately 0.5 Å.
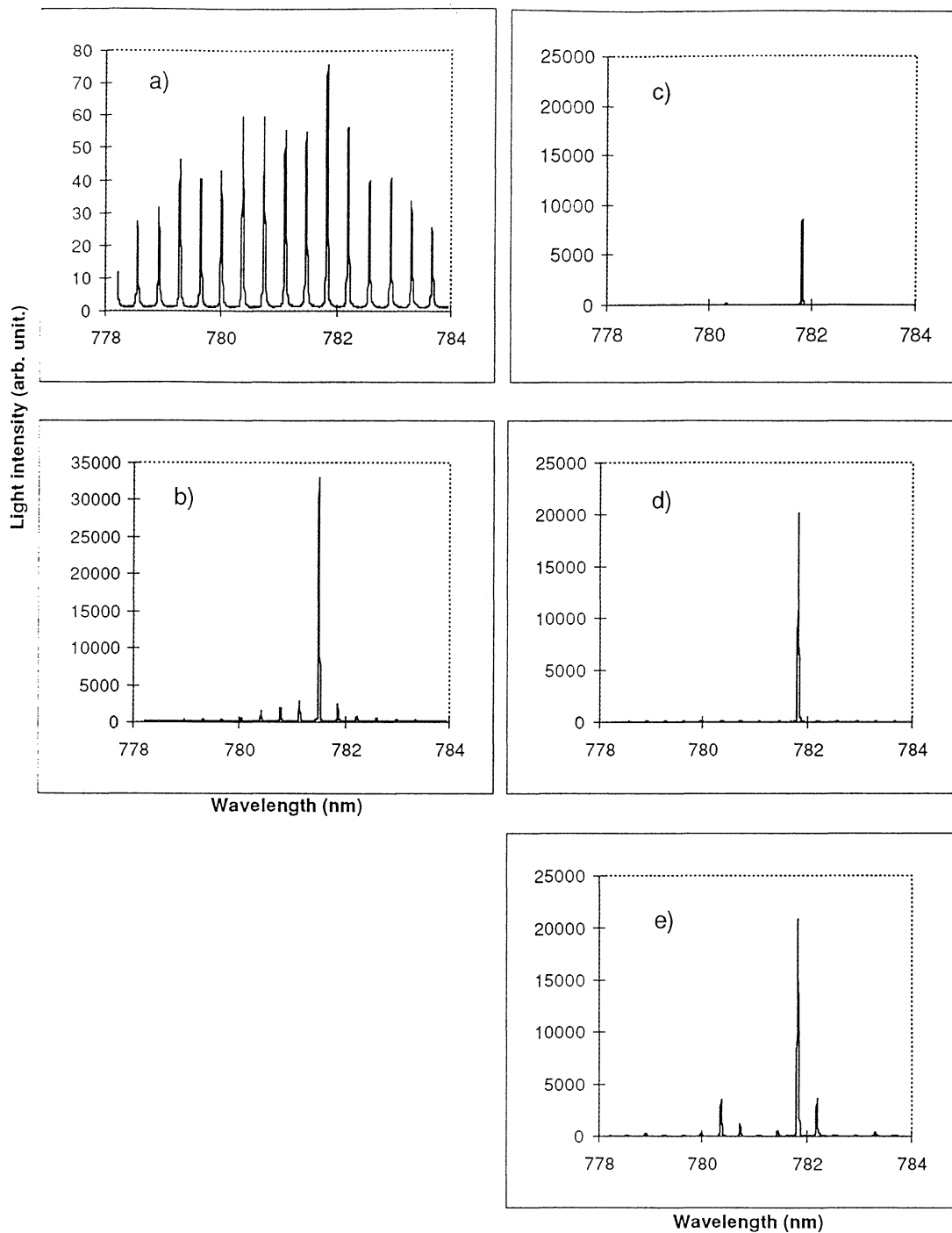
Fig. 2.6 *Optical spectra for the solitary diode (a) and (b), and for the external cavity coupled diode (c)-(e), recorded at the operating points indicated in Fig. 2.5. The spectra in (a), (b) and (e) display multi-mode behaviour, while the spectra in (c) and (d) are single-mode.*

The wavelength separation between neighbouring longitudinal modes, given by Eq. (1.2), can be used to evaluate the diode cavity length. The length was evaluated to 273 μm.

Notice the strong dependence of the optical spectrum on the operating point along the P-I characteristic. At low currents, the spontaneous emission has broad spectral distribution, while above the threshold current the laser approaches single-mode radiation.

It can be concluded that the frequency and the output power of the emitted light can be effectively controlled by means of injection current and temperature.

2.1.2 The external cavity

The external cavity laser is build up with a minimum amount of components. It consists of a laser diode, a collimating lens, and an external mirror, all mounted on an optical rail to make a stable feedback optics. The external cavity length can be varied by translating the mirror along the optical rail. The external mirror is mounted upon a standard mirror mounting with fine adjustment screws. The alignment of the external cavity was a rather complex procedure in that the different elements were added successively and then appropriately adjusted by making use of the diagnostic instruments.

Part of the laser emission is reflected back from the external mirror, and by passing once again through the collimating lens, gets back into the diode resonator and interacts constructively with the field in it. An extremely accurate coupling of the backscattered light into the ca. 1×5 μm aperture of the active strip is needed [33].
The principal optical losses occur at the coupling of the reflected feedback via the collimator back into the diode cavity. It is plausible to assume that, partly due to a certain unevenness of the external mirror and partly due to the astigmatism of the emitted laser light, only the central region of the collimated beam is readily coupled back into the diode cavity. This part of the beam has the highest light intensity and suffers the least from aberrations.

The coupling of the reflected light back into the laser cavity is controlled by the focusing of the collimating lens and the tilt of the external mirror. As a practical concern, the external mirror was aligned by reducing the injection current to just below the solitary diode threshold and adjusting the mounting screws, until a strong light output power increase is recorded and the laser mode hoping becomes very sensitive to the optical feedback. The geometry of the system was optimised so as to maximise the output light intensity and to obtain single-mode radiation. The emitted beam should have an essentially Gaussian intensity profile. The highest feedback levels turned out to be extremely difficult to reproduce.
Poor alignment yields an unstable operation, which is characterized by multiple external cavity modes and a noisy light output in the form of statistically distributed intensity breakdowns.

The behaviour of the system was found to be critically dependent on the detailed experimental conditions. For instance, the compound laser was extraordinarily sensitive to misalignment or fine adjustments of the external optics which fixes the light distribution on the laser facet. A minute change of the planar external mirror tilt or of the collimating lens focusing could result in dramatically different spectra.

The stability problems caused by environment disturbances were of crucial practical concern. A series of steps were taken in order to reduce the effects of mechanical vibrations, e.g. the whole experimental set-up was placed on a heavy optical bench and all vibrating electrical instruments were removed. To protect the external cavity from turbulence of the air, causing temperature variations and refractive index gradients along the optical path, the feedback arm was carefully isolated using a cardboard shielding (see Fig. 2.1). Additionally, precautions were taken to prevent inadvertent optical feedback from other elements.

Selection of the operating parameters. The operating point of the diode system is specified by the following parameters: the external cavity length, the reflectivity of the external mirror, the injection current, and the temperature of the semiconductor material. All these parameters influence the optical properties and the stability of the laser. An extensive series of tests was performed (interactively varying length, reflectivity, current and temperature) in order to arrive at an optimal operating point for aerosol measurement.

The light emitted by a laser is coherent, i.e. the stimulated photons have the same frequency, phase and direction of propagation [7]. A characteristic of coherent light is that it interferes, while incoherent light does not. Hence, the maximal interaction between the laser field inside the diode cavity and the reflected waves takes place if coherence occurs [27,28]. This state is then characterized by the presence of a single resonant mode and a stable output intensity. In this case the system behaves as a compound cavity laser. Since the light must travel back and forth within the external cavity, the distance from the emitting diode facet to the external reflector should not exceed a half of the coherence length.

It was experimentally found that the external cavity becomes more difficult to align for single-frequency operation as the length of the cavity increases. For long external cavity lengths, a drastic increase of intensity noise was observed in which the laser suddenly switched to the so called *coherence collapse* region [8,28,31,34].

The "coherence collapse" regime is characterized by multiple external cavity modes, spectral linewidths of several tens of gigahertz, and a large intensity noise. The coherence collapse is usually attributed to a switching phenomenon, between the behaviour of the system operating as a coherent compound cavity and its operation as a solitary laser with a disturbing optical feedback. In this regime, the external cavity laser may be a good candidate for observation of optical chaos [28].

Reduction of the external cavity length stabilised the laser diode and resulted in low intensity noise. The *external cavity length* was finally chosen to $L_E = 75$ *mm*, which was the minimum length achievable with the present set-up.

The feedback rate was controlled by means of the reflectivity of the external mirror. Experimental and theoretical results reported by [28,34] show that a phenomenological classification in different feedback regimes can be made, characterized by the external cavity length L_E and the external mirror reflectivity R_{ext}. For external cavity lengths of the order of 100 mm, stable feedback conditions can be achieved for either low feedback (typically $R_{ext} <$ 1%) or, alternatively, for strong feedback ($R_{ext} > 20\%$). However, in the second case it is necessary to antireflection coat the front facet of the laser [28,31]. In the moderate feedback regime ($\approx$ 1-20% reflectivity), "coherence collapse" will result. The experiments performed have confirmed this expected behaviour. The highest stability of the output intensity, and the strongest single-mode behaviour could be achieved with an uncoated glass plate. Thus, the *external mirror reflectivity* was, according to Fresnel's equation, $R_3 \approx 8\%$. (This was in fact the lowest available reflectivity.) The feedback of light into the diode cavity is estimated using a coupling efficiency η to obtain $R_{ext} = \eta R_3$ (compare with Sect. 1.3.2). Due to a presumably low coupling efficiency η, the effective external reflectivity R_{ext} corresponded to the week feedback regime. Coupling efficiencies of around 0.1-0.3 have been estimated [19,20,33], depending for instance on the external mirror quality. (It may also be possible that the glass plate, which had a rather poor optical quality, only coupled back light reflected from *one* of the reflecting surfaces, which implies an external mirror reflectivity $R_3 \approx 4\%$.)

From the shape of the light output power versus injection current characteristics (see Fig. 2.5), it can be seen that an effect of the external reflection is the reduction in the threshold current. This is caused by the additional gain supplied by the external feedback (compare with Eqs. (1.12) and (1.25)). At poor alignment, there will be a smooth kink in the vicinity of the solitary laser threshold [17,28].

Given the variations of the threshold current I_{th} as a function of optical feedback, the alignment of the external cavity may be optimised by minimizing the threshold current of the compound cavity $I_{th,e}$. By reducing $I_{th,e}$ as much as possible, the laser becomes very sensitive to disturbances in the optical feedback. This, in turn, is advantageous by the use of the compound cavity system for aerosol measurement.

The threshold current obtained employing the external mirror of reflectivity $R_3 \approx 8\%$ at the temperature $T = 20.75$ °C was $I_{th,e} = 18.2$ mA (see Fig. 2.5). It means a reduction of ca. 6% ($I_{th,s} = 19.4$ mA, compare with Sect. 2.1.1). The threshold current reduction was comparatively small, and therefore one could conclude that the coupling efficiency η was relatively low.

The emitted light spectrum is highly dependent on the operating point along the characteristic, as can be seen in Fig. 2.6c-e. (The graphs correspond to the operating points indicated in Fig. 2.5.) As mentioned in Sect. 1.3.2 the external cavity configuration allow for supression of subsidiary longitudinal modes, i.e. single-mode emission. At the operating point (e), that is slightly above the threshold current for the solitary diode, the single-mode behaviour deteriorates. This can be explained in the following way [28]:

When a semiconductor laser with an external mirror is operated below solitary laser threshold, i.e. $I_{op} < I_{th,s}$, coherent optical interference effects between the field inside the laser diode and the light reflected from the mirror are necessary for the laser to work. The system has then to be considered as a laser whose amplifying medium is placed at the end of the resonator cavity. The compound cavity is then delivering a stable intensity output and the optical spectrum is single-mode. Beyond solitary laser threshold, i.e. $I_{op} > I_{th,s}$, the laser diode operates as an autonomous system. The laser oscillation takes place between the end facets of the diode, and the external mirror acts as a disturbance. This yields an unstable, noisy intensity output. The average intensity output decreases and the competition of oscillating modes results in a multi-mode emission. Hence, the *operating current* was set to *$I_{op} = 18.9$ mA*, i.e. between $I_{th,s}$ and $I_{th,e}$. At this point coherent interference in the three-mirror cavity occurs. I_{op} was also chosen to be as low as possible (still preserving the single-mode behaviour), in order to increase the sensitivity of the lasing system to external disturbances.

As discussed in Sect. 1.3.2, the laser oscillation conditions are changing with short-range variations of the temperature in the semiconductor crystal. The emission wavelength of a semiconductor diode laser can thus be tuned by varying the temperature of the laser chip.

The goal was to set the temperature (by means of the Peltier element) so that the single-mode frequency emitted by the external cavity system coincides with that of the solitary diode at injection current levels above $I_{th,e}$. The influence of the longitudinal subsidiary modes is then minimised. The *temperature* was accordingly chosen at *20.75 °C* so that the emission wavelength of the compound cavity system (almost) coincides with that of the solitary diode (as illustrated in Fig. 2.6).

To sum up, at an operating point given by the injection current I_{op} = 18.9 mA, and with the semiconductor laser stabilised at the temperature T = 20.75 °C, the light output power was about 150 µW. The emitted light was single-mode with a wavelength of 781.84 nm.

Under these conditions, the system was stable for a few minutes and measurements on particles could be performed. The coupled cavity system was also very sensitive to external disturbances.

2.1.3 The optics

As discussed in Sect. 1.4, by collecting the scattered light in the near-forward direction where the diffraction part dominates, the influence of the refractive index is minimised and the particle size can be determined using the Fraunhofer approximation.

The optical set-up used for recording of the diffraction pattern consists of three lenses (L1, L2, and L3) and a CCD camera as shown schematically in Fig. 2.7.

The condition for the Fraunhofer diffraction is that the observation is made in the far-field region, i.e. R >> d^2/λ (see Sect. 1.4). However, one can introduce a lens L1 behind the particle in order to shorten the distance to the image plane. This lens is referred to as the transform lens, since it generates an instant *Fourier transform* at its back focal plane. In fact, the Fraunhofer diffraction pattern is identical to the Fourier transform of the field distribution across the scatterer performed by the transform lens [26]. Hence, the far-field diffraction pattern of the particle is spread across the back focal plane of the transform lens.

If more than one particle is located in the illuminated sensing volume, then the light intensity distribution on the focal plane is the sum of the contributions from the individual particles.

It is interesting to note that the image of the particle will be formed by the transform lens L1 on the conjugate plane to the object plane, in our case at infinity since the particle is located in focus (see below).
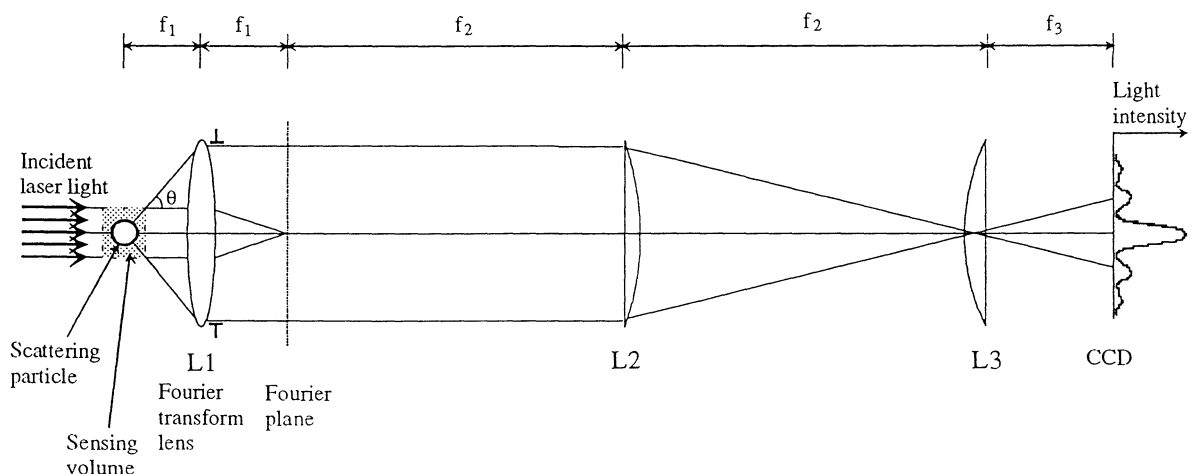
Fig. 2.7 *Optical arrangement with a Fourier transform lens, used to determine the size of light scattering particles. The bi-convex lens L1, and the two plano-convex lenses L2 and L3 have focal lengths f_1 =40 mm, f_2 = 300 mm, and f_3 = 100 mm, respectively. They are all Ø 21.5 mm. The beamprofiler CCD camera has an imaging area of 5.45 (H) ×6.14 (V) mm.*

The Fourier transform lens L1 collects both the near-forward scattered light from the particle, and the primary laser beam. At the back focal plane of the lens, unscattered light is focused to a point on the optical axis, while the scattered light forms a diffraction pattern around this central spot (actually it is centred about the axis of the Fourier transform lens). As the receiving lens performs a Fourier transform on the scattered light, diffracted light at an angle θ will always give the same radial displacement in the focal plane, irrespective of the particle's position in the illuminating beam. Thus, the resulting pattern is unaffected by the particle location or motion.

By means of a spot dump located in the back focus of lens L1, the primary laser beam is separated from the light scattered by the particles. Without this spatial filtering, the intense primary light would totally obscure the much weaker scattered light.

The Fraunhofer diffraction pattern in the Fourier plane is subsequently reduced by the two lenses L2 and L3, in order to be imaged on the limited sensing area of the CCD chip (see Sect. 2.1.4). Thereby, the light is passed via a beam-splitter to the CCD camera. The optics are arranged so that the back focal plane of lens L1 coincides with the front focal plane of lens L2. The CCD camera is located at the back focal plane of lens L3 (see Fig. 2.7). Hence, the total transverse magnification of the compound lens system L2 and L3, is given by [26]

$$M_T = \frac{f_2 s_{i3}}{d(s_{o2} - f_2) - s_{o2} f_2} = -\frac{1}{3},$$ (2.3)

where s_{o2} is the object distance of the compound lens, here equal to f_2, and s_{i3} is the image distance equal to f_3. d is the distance between L2 and L3.

Due to spherical aberrations introduced by the focusing lens L1, there is an insufficient spatial filtering by the spot dump. A lens is used to collimate the leakage light into a beam of parallel rays which is directed towards the entrance slit of the spectrometer for monitoring of the emission spectrum (see Fig. 2.1). There is also a leakage of primary light onto the CCD camera (see Fig. 2.8). This makes necessary the use of a neutral density filter, located in front of the monitoring CCD camera. By recording of the diffraction pattern of the particles, background subtraction was applied.

The angle range of the scattered light collected by the optics is determined by the numerical aperture of lens L1 and the diameter of the spatial filter placed in the back focus of lens L1. In our case, scattered light in the near-forward direction at coaxial semi-angles between 2° and 10° is collected.

Because the aperture of the transform lens L1 is not large enough to collect all the diffracted light, the higher spatial frequencies associated with the outer region of the Fraunhofer pattern will be lost. Thus, the transform lens L1 simultaneously functions as a low-pass filter of spatial frequencies.

As a practical concern, the scattering particle should be located within a maximum allowable distance of the receiver Fourier transform lens. If the particle is further away than this, it may scatter light beyond the receiving lens. This effect is called *vignetting* [2,25]. Vignetting affects preferentially the diffraction of the smallest particles, since they scatter the light at the largest angles.

Fig. 2.8 *Image on the monitoring CCD camera of the laser light transmitted through the imaging optics. This light leakage, due to insufficient spatial filtering by the spot dump, make the use of a neutral density filter (transmittance T = 0.3) necessary. This also substantially reduces the intensity of the scattered light. By the recording of scattered light, background subtraction was performed.*

One of the most difficult aspects of making an accurate *in situ* measurement is in defining the *sensing volume*, as particle velocities and trajectories cannot be controlled. The sensing volume is determined by the intensity profile of the illuminating beam and by the geometry and characteristics of the receiving optics.

In our case, the sensing volume is limited in principle by the cross-section of the laser beam and the whole extent of the external cavity. However, due to the influence of vignetting, it must be reduced to a small region along the beam axis centred around the focus of lens L1 (see Fig. 2.7).

2.1.4 The detection system

Light emitted from the back facet of the laser diode falls onto a *photodiode* (*PD*), which is equipped in the LD package (see Fig. 2.3a). This makes a very compact and user-friendly set-up. The photodiode transforms the measured light into a voltage signal which is proportional to the light flux.

The output signal is then analysed by a fast *digitising oscilloscope* (Tektronix TDS500B). In this way, the output light intensity is monitored and the time variation can easily be plotted.

As already mentioned, the near-forward scattered light is imaged on a infrared sensitive *charge-coupled device* (*CCD*) *camera*. A CCD is a solid state two-dimensional array detector composed of a matrix of light sensitive elements [30]. Some of the properties of the employed CCD camera are listed in Table 2.2 below. The CCD camera was controlled by a software acquisition and data handling program.

Table 2.2 *Properties of the CCD camera.*

Device	Type	Spectral response (nm)	Sensor elements (full res.)	Pixel size (μm)	Imaging area (mm)
Cohu 4800	Frame transfer CCD	190-1100	377 (H) × 244 (V)	23.0 (H) × 27.0 (V)	5.45 (H) × 6.14 (V)

The output voltage from the monitoring photodiode is coupled to a *signal discriminator* device used to set the trigger level. It can send electric pulses (duration ca. 400ns) which simultaneously trigger the oscilloscope and the monitoring CCD camera. Thus, diffraction images of the disturbing aerosol particle can be synchronized with plots of the variation of the optical output power (see Sects. 3.1 and 3.2).

2.2 The samples

For a simulation of aerosol particles, the experimental evaluation was conducted on fibres of different materials and diameters. The source of the fibres was reinforcement fabric used in orthopaedics. These fibres are produced commercially mainly for use in high-strength products. The dimensions of the fibres were measured with a standard optical microscope. A glass fibre with a diameter of 5.6 μm represented the minimum sampling size. The other fibres were: single carbon fibre (7 μm), twisted double carbon fibre (14 μm), kevlar fibre (12 μm), nylon fibre (34 μm). All these fibres can present potential health hazards. Furthermore, the light pattern from the highly dangerous asbestos fibre is quite similar to that from e.g. a glass fibre of same diameter [2]. The glass and the mineral fibres were found to be nearly cylindrical, while the nylon fibre presented a particularly rough surface. The fibres were mounted on simple holders, in order to enable careful control of their exact position inside the external cavity.

2.3 The experimental measurements

The fibres were passed through the sensing volume, orthogonally to the laser beam direction. The scattered light was then dispersed into a plane perpendicular to the fibre axis. It is important that the fibres are held perpendicularly to the beam axis in order to obtain the characteristic diffraction pattern described in Sect.1.4.

As some practical concerns, the light was switched off while the samplings of wavelength spectra and of diffraction images were carried out, so as to minimise the stray light into the detection system. The entrance slit of the spectrometer was limited even in the vertical direction, in order to avoid scattered light which disperse along that direction to influence the measured intensity variation of the transmitted light (compare with Fig. 3.9).

In order to improve the signal-to-noise-ratio, a low-pass filter was employed on the monitoring voltage signal from the photodiode so as to filter away high frequency variations caused by mechanical vibrations and electrical disturbances.

3. Experiment evaluation

3.1 The diffraction pattern

A fibre generates a diffraction pattern consisting of a series of dashes of light lying along a straight line perpendicular to the fibre direction and passing through the optical axis. The thinner the scattering fibre, the larger the angular spread of the diffracted beam. The strength of the scattering intensity varies also strongly with the fibre size (see Sect. 1.4).

The recorded images and the cross-sections of the scattered light distribution obtained from the different fibres is shown in Fig. 3.1. The scattering angle is presented at the bottom of the figure. The intensity distributions were integrated by summing over a series of cross-sections taken along the diffraction patterns. Notice the well-defined scattering pattern of the uniformly thick glass and single carbon fibres, while the rough surface or uneven thickness of the other fibre samples produced a more diffuse structure (with non-zero irradiance minima). The central missing region corresponds to the spatial filtering by the spot dump, while the gradual fading out of the diffraction pattern and its final truncation is caused by the vignetting (compare with Sect. 2.1.3).
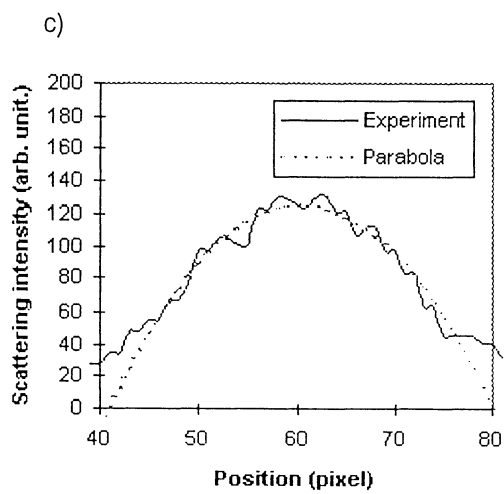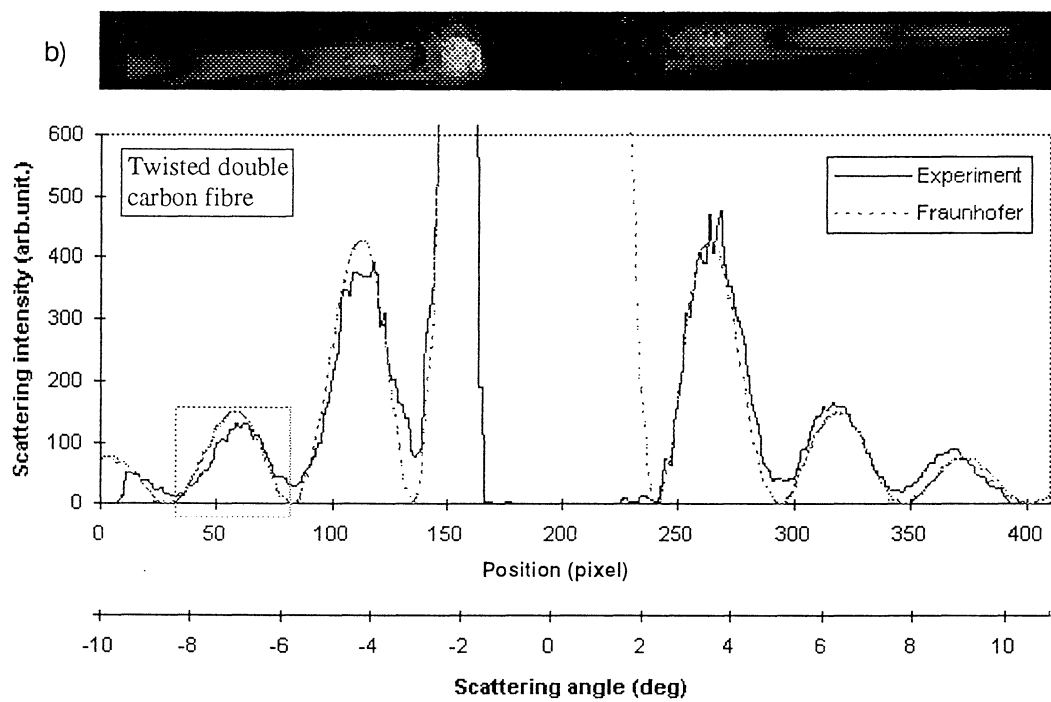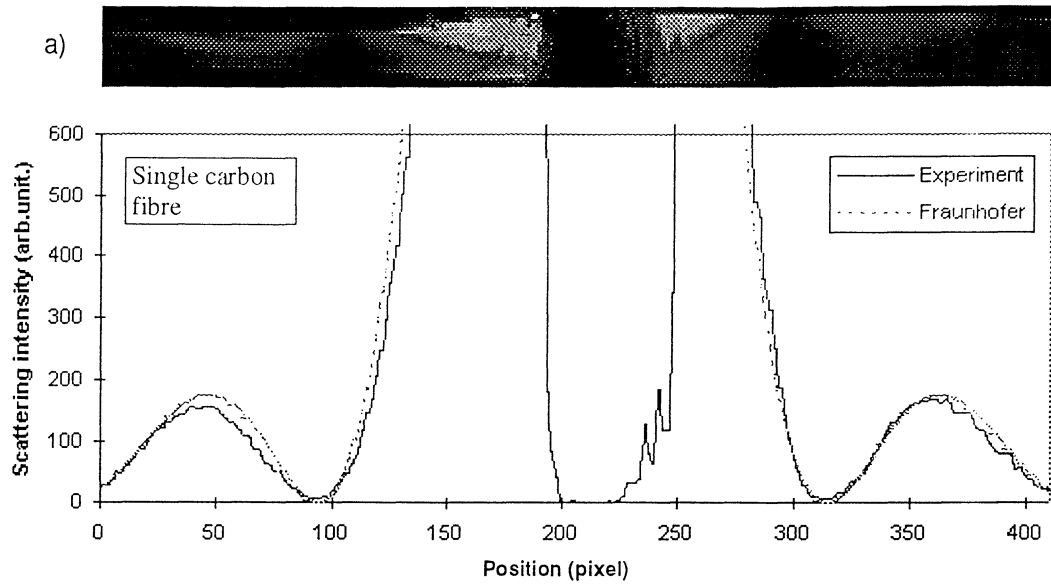
The fibre sizes were determined from the measured intensity distribution data by best-fitting reconstruction methods, assuming Fraunhofer diffraction. Two methods were employed: one is to fit a Fraunhofer curve to the recorded intensity data by optimising the input parameters (the results are illustrated as the dashed lines in Fig. 3.1); the other makes merely use of the positions of the intensity minima and maxima.
By the intensity fit method, the fibre sizes were evaluated from the fitted parameters.
In order to evaluate the fibre dimensions using the minima and the maxima positions in the recorded intensity distribution, parabolas were first fitted to every maximum and minimum of intensity, respectively. An example of the resulting fit is shown in Fig. 3.1c. The obtained pixel positions of the extrema are listed in Appendix C. The corresponding orders of maxima and minima were then pared together in order to evaluate the distance between two successive minima. It should be noticed that the spatial frequency of the minima in the Fraunhofer diffraction pattern is equal to the spacing between the zeroth order and the first minimum. Thus, through geometrical considerations and using the notations in Fig. 3.2, the following expression for the scattering angle corresponding to the first intensity minimum is arrived at

$$\theta_1 = \arctan\frac{3\Delta}{40}.$$

(3.1)

Fig. 3.1 *Recorded diffraction patterns of single fibre samplings: single carbon fibre (a), twisted double carbon fibre (b), kevlar fibre (d), nylon fibre (e), and glass fibre (f). The triggered images recorded with the monitoring CCD camera are shown at the top. Below, cross-sections of the diffraction images are presented (solid line). The dashed lines represent the fitted Fraunhofer distributions. An enlarged section of the intensity distribution for the twisted carbon fibre, between pixel 40 and 80, is shown in graph (c). This should exemplify the procedure of fitting parabolas to the experimental data, in order to derive the position of the extrema values.*

a)

Single carbon fibre

Experiment
Fraunhofer

Scattering intensity (arb.unit.)

Position (pixel)

b)

Twisted double carbon fibre

Experiment
Fraunhofer

Scattering intensity (arb.unit.)

Position (pixel)

Scattering angle (deg)

c)

Experiment
Parabola

Scattering intensity (arb. unit.)

Position (pixel)

d) Kevlar fibre

Legend: Experiment (solid), Fraunhofer (dotted)

Y-axis: Scattering intensity (arb.unit.)
X-axis: Position (pixel)

e) Nylon fibre

Legend: Experiment (solid), Fraunhofer (dotted)

Y-axis: Scattering intensity (arb. unit.)
X-axis: Position (pixel)

f) Glass fibre

Legend: Experiment (solid), Fraunhofer (dotted)

Y-axis: Scattering intensity (arb. unit.)
X-axis: Position (pixel)

Scattering angle (deg)

By employing Eq. (1.39) with the parameter m = 1, the relation for the fibre dimension can be written as

$$d = \frac{\lambda}{\sin\theta_1} \, .$$

(3.2)

Combining Eqs. (3.1) and (3.2), we finally get an expression for the relationship between the fibre diameter d and the spacing between intensity minima Δ.

The results from the computations using the intensity fit and the fit by the positions of intensity extrema, respectively, are shown in Table 3.1. A size evaluation for the glass fibre using the extrema fit was not possible due to the limited scattering angle range.

Table 3.1 *Comparison between evaluated values of fibre diameter obtained by best-fitting reconstruction assuming Fraunhofer diffraction, and measured values using an optical microscope.*

Fibre sample	Measured dimension (μm)		
	microscope	intensity fit	extrema fit
glass fibre	5.6	(5.2)	—
single carbon fibre	7	8.2	7.00 ± 0.04
twisted double carbon fibre	14	17	14.67 ± 0.14
kevlar fibre	12	16	14.03 ± 0.28
nylon fibre	34	41	34.56 ± 0.72

The quite bad quality of the diffraction images (possibly due to lens aberrations — compare with Sect. 4.1) is mainly affecting the size evaluation based on scattered light intensity distribution. It might partly explain the overestimation of the fibre diameters obtained with this method.

On the other hand, the values obtained by fitting to the irradiance maxima and minima correspond very well to the measurements made under microscope.
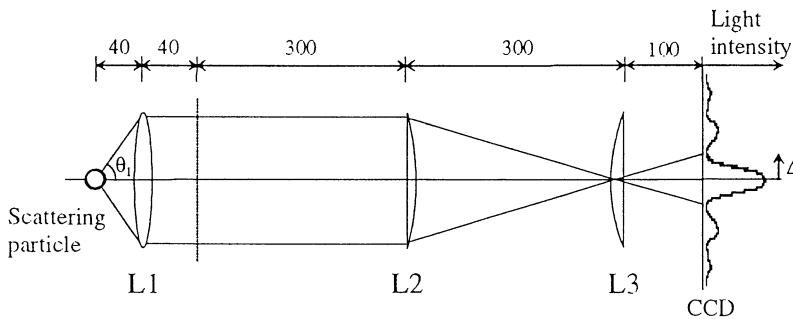
Fig. 3.2 *Ray optics for computation of particle dimension, using the first irradiance minimum in the Fraunhofer diffraction distribution. θ_1 denotes the scattering angle and Δ is the distance from the center, both parameters corresponding to the first intensity minimum.*

3.2 The output light intensity

The triggered photodiode voltage recordings were evaluated, after being transferred to a personal computer, using the analysis software Excel 7.0.
Typical time-traces of the photodiode output voltage, corresponding to samplings of the different fibres, are shown in Fig. 3.3 and Fig. 3.4. The grey dashed lines represent the registered photodiode (PD) voltage, while the black solid lines correspond to filtered signals obtained by averaging the output voltage of every pixel with its surrounding ten neighbouring pixels.

From the time-resolved output voltage recordings shown in Fig. 3.3, corresponding to light intensity variations in the laser system, one can see that the samplings on glass, kevlar and nylon fibres show a marked reduction of light intensity as the fibres enter or leave the external cavity. We define this drop-off as the *edge signal*. With the fibres well inside the laser beam, the light output increases again and remains relatively constant until a new drop-off is registered as the fibres leave the sensing volume. Below, a possible model will be formulated, which might explain the observed phenomenon.

The scattering and absorbing properties of the particle are influencing the optical output of the diode system through the particle's interaction with the laser light inside the external cavity. Initially, as the scattering particle comes in tangentially to the beam, the main effect on the lasing system is caused by diffraction which concentrates the light within the forward scattering lobe. However, as discussed in Sect. 1.4, the perturbation of the electromagnetic field goes beyond the physical presence of the scatterer. This means that the part of the laser beam passing along the edge of the particle becomes decollimated and will not be coupled back into the diode cavity. This leads to increased losses for the lasing system and to a consequent reduction of the output light intensity.
It should also be considered that the incident laser light striking the particle is not homogeneous, but has essentially a Gaussian intensity profile. This means that the particle entering the laser beam encounters the flank of the intensity distribution first, absorbing peripheral light with low intensity and, at the same time, deflecting light at the beam centre, with much higher intensity. Thus, the initial decollimation of the beam, and the resulting drop-off of the output intensity, can mainly be seen as an effect of light diffraction.

As the particle is positioned well inside the laser beam, although still deflecting the laser light, its forward and backscattered light (corresponding to scattering angles $\theta = 0°$ and $\theta = 180°$) will readily be coupled back into the amplifying cavity and thus reinforce the lasing. This effect can be seen as if the particle was "focusing" the scattered light (mainly) in the forward direction, i.e. into the diode cavity. Hence, the light intensity will increase.
At the same time, the absorbing properties of the particle, controlled by the refractive index of the material, will cause a portion of the collimated beam of light to be removed. This amount of absorbed light is also proportional to the projected area of the particle, and thus to the particle size. The backscattered light, due to reflection, is also influenced by the particle's shape. On the way out of the laser beam the particle will once again decollimate the beam and a new intensity decrease will occur.
A simple model for the dynamic interaction of aerosol particles with the light inside the external cavity is depicted in Fig. 3.5.
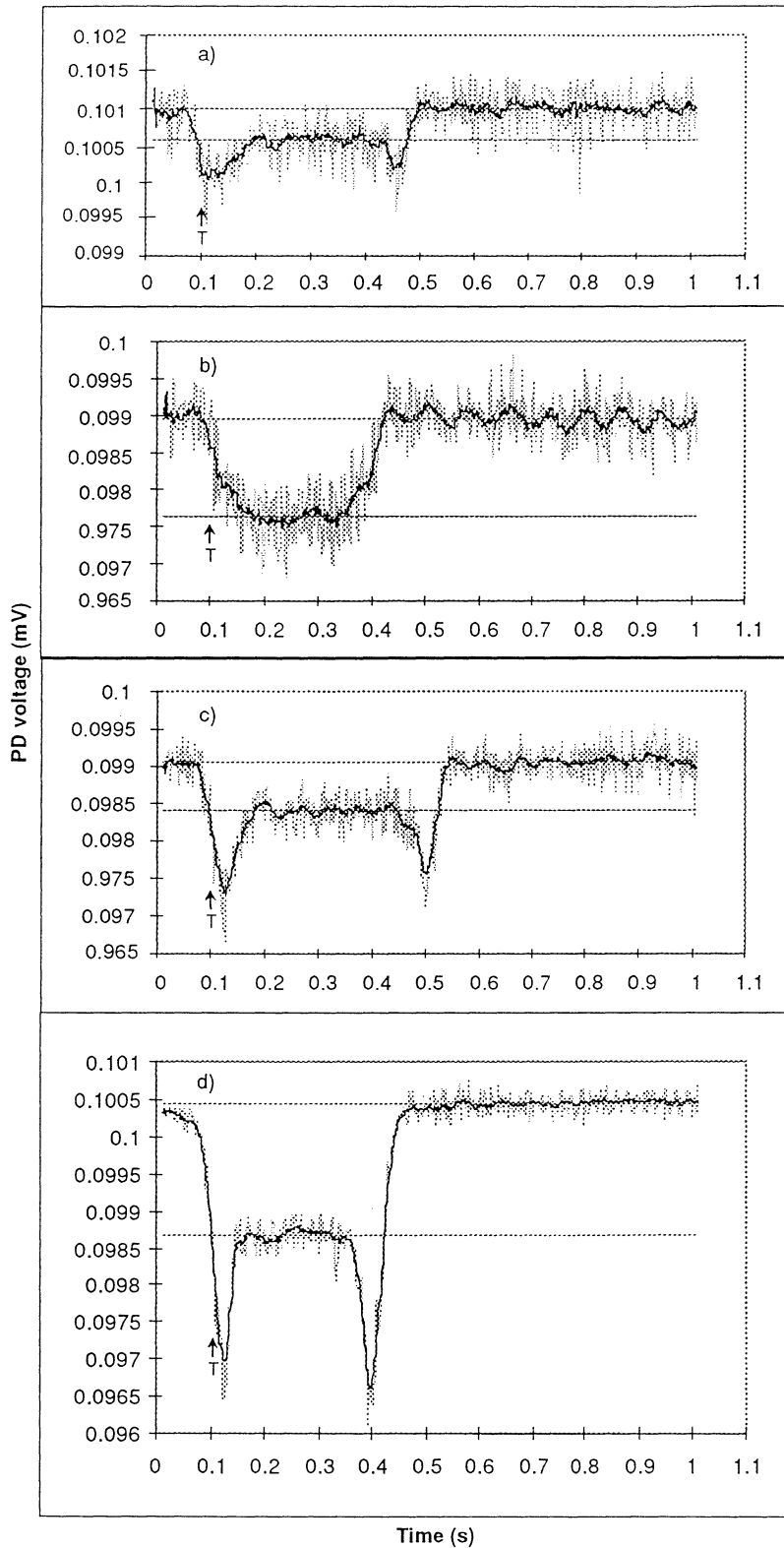
Fig. 3.3 *Time-trace of the output voltage from the monitoring photodiode (PD), corresponding to the measured oscilloscope signal from a single fibre moving through the external cavity. The recordings are from a glass fibre with a diameter of 5.6 μm (a), a twisted double carbon fibre of 14 μm (b), a kevlar fibre of 12 μm (c), and a nylon fibre of 34 μm (d). The arrows at the time t = 0.1 s mark the onset of the trigger.*
Notice that the output voltage levels in the undisturbed state (straight solid line) vary between the measurements. This is due to the inherent instability of the compound lasing system, easily affected by external disturbances, such as mechanical vibrations.

Examining the time-resolved trace of the recorded output PD voltage (see Fig. 3.3), we observe that the edge signal, i.e. the intensity fall-off registered as the fibres are being introduced or removed from the laser beam, increases with increasing fibre dimensions.
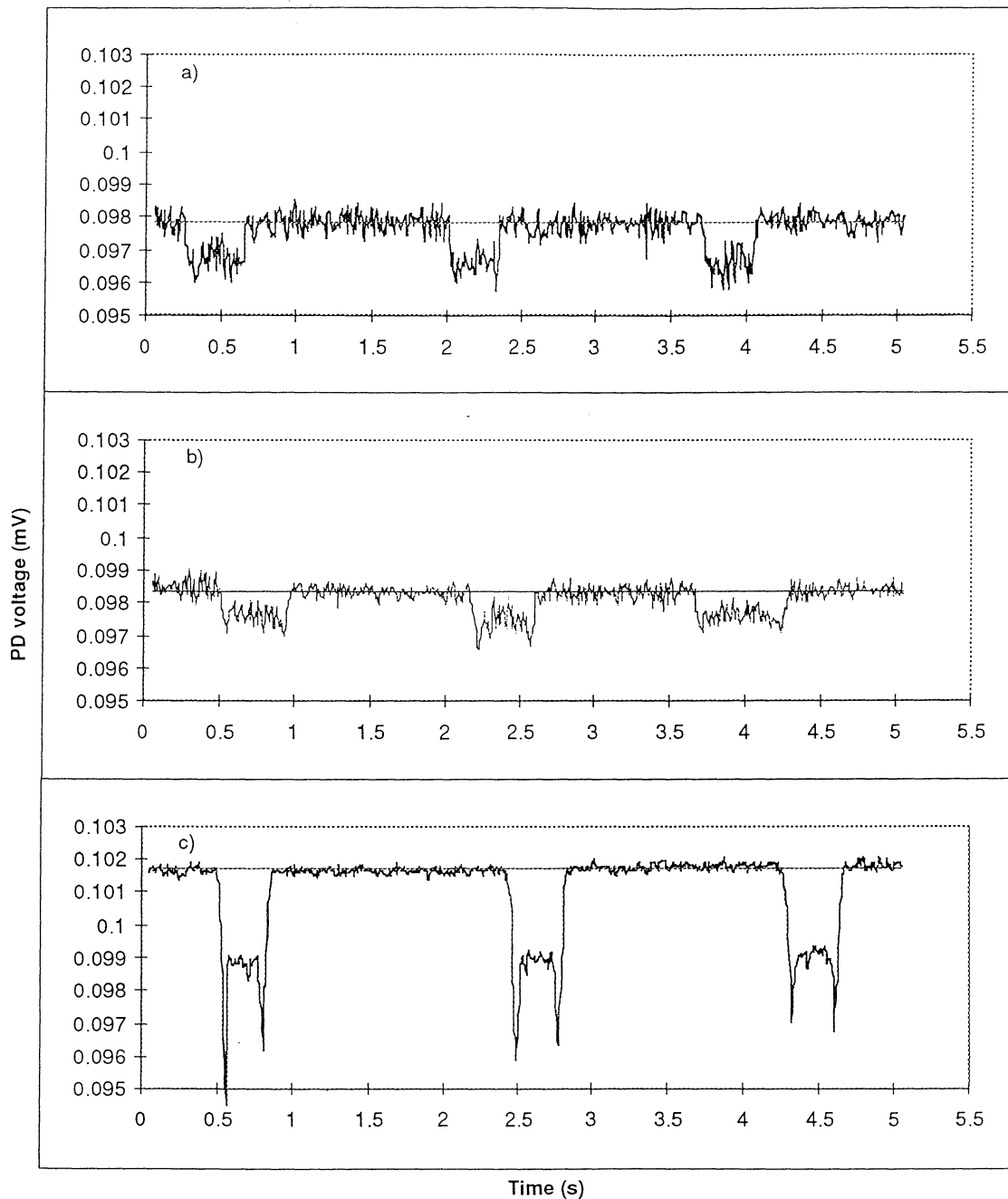
Fig 3.4 *Time-trace of the output photodiode (PD) voltage from multiple consecutive samplings on fibres: (a) carbon (14 µm), (b) kevlar (12 µm), (c) nylon (34 µm).*

This seems to agree with our assumption that the edge signal is principally an effect of diffraction, since, in accordance with Mie scattering theory (see Sect. 4.1), the intensity of scattered light is proportional to the projected area of the particle.

The dependence of measured edge signal on the size of the fibre for the glass, kevlar and nylon fibres is shown in Fig. 3.6 (the markers correspond to several different measurements). The signal amplitude increases linearly with particle diameter. The mean values and standard deviation of this signals are tabulated in Table 3.2. Notice the large value of the edge signal for the nylon fibre, which also has the largest diameter (d = 34 µm). The edge features for carbon are not clearly discernible, and are therefore not presented.
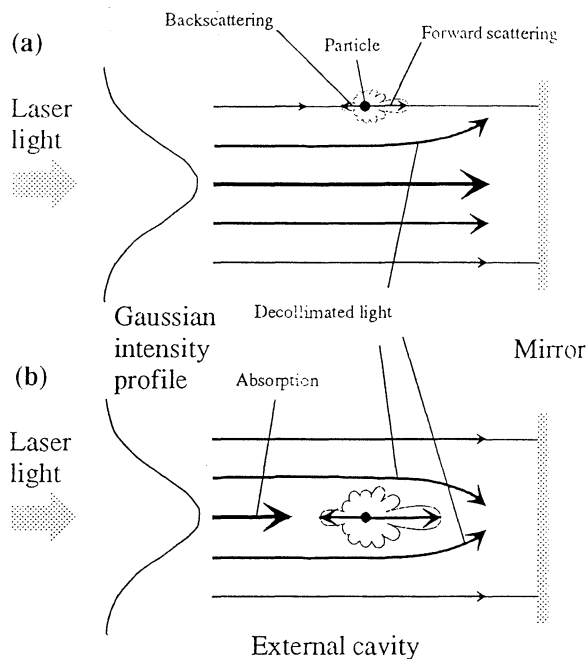
Fig. 3.5 *A model for the dynamic interaction between an aerosol particle and the laser light inside the external cavity. The aerosol particle just coming into the laser beam (a), and moving inside the beam (b). For clarity of presentation, the back-coupled light has been omitted in the figure.*

The level of the intensity "plateau", corresponding to fibres moving inside the laser beam and mainly determined by the absorption, is a function of fibre diameter and refractive index of the material. We call it the *inner cavity signal*. The transparent glass fibre, and the semi-transparent kevlar and nylon fibres exhibit relatively low inner cavity signals, due to their limited absorption. Carbon, on the other side, is a highly absorbing material, and does not show any intensity increase as the fibre is moving inside the laser beam. One can possibly distinguish a further intensity decrease. In this case the absorption is believed to dominate over the effect of scattering. A plot of the measured inner cavity signals for the glass, kevlar, twisted double carbon, and nylon fibres is shown in Fig. 3.7, and the mean values and standard deviation of this signals are tabulated in Table 3.3. The rather large variation of the signal amplitude in this case (compared with the edge signal) can be attributed to the superposed effect of the fibre size and the refractive index of the material.

The time-trace of the output PD voltage variation by sampling, gives information about the velocity of the fibre. It can be derived by dividing the height of the sensing volume, through which the fibre is moving, by the time-of-flight. From Fig. 3.3 and Fig. 3.4 a time-of-flight of 0.3 s is estimated, and given the height of the laser beam of 4 mm (see Sect. 2.1.1), one arrives at a velocity for the fibres v ≈ 1 cm/s.

3.3 Instrument diagnosis

For diagnostic purposes, the emitted light spectra from the compound cavity laser were analysed in both undisturbed condition and with a fibre located in the external cavity, respectively. A typical recording is shown in Fig. 3.8.

At stable lasing conditions, i.e. with an optimum alignment of the external cavity and with operating parameters chosen so that single-mode emission and low output power noise are achieved (see Sect. 2.1.2), the fibre disturbance merely causes a reduction of the light intensity at the single-mode peak. The faint subsidiary longitudinal modes are then unaffected.
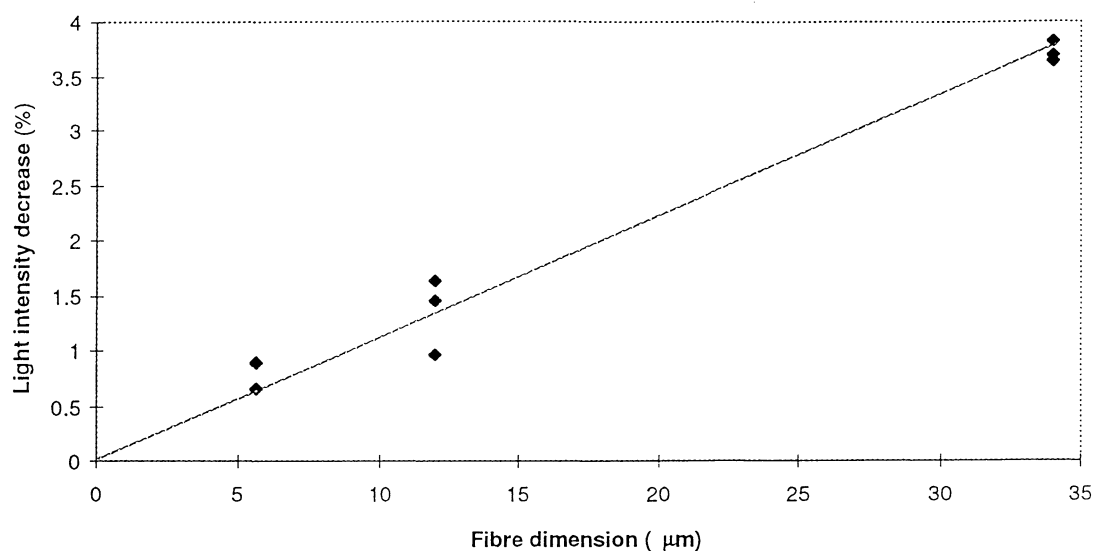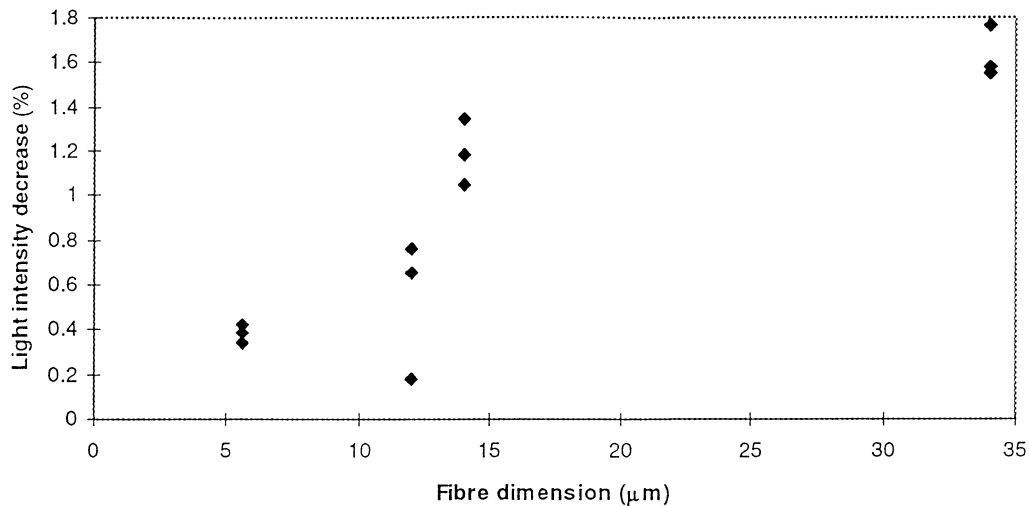
Fig. 3.6 *Plot of the measured output light intensity decrease as a fibre enters, respectively leaves, the external cavity beam. We define it as the edge signal. The square markers correspond to measurements on: glass fibre (5.6 µm); kevlar fibre (12 µm); nylon fibre (34 µm). A linear regression fit was performed, shown as the adjacent dashed line.*

Table 3.2 *The measured output light intensity decrease as a fibre enters, or leaves, the external cavity beam, here defined as the edge signal.*

Fibre sample	Fibre dimension (µm)	Light intensity decrease (%)	Mean value (%)	Standard deviation (%)
glass fibre	5.6	0.90	0.81	0.14
		0.66		
		0.89		
kevlar fibre	12	0.97	1.35	0.35
		1.64		
		1.46		
nylon fibre	34	3.69	3.71	0.09
		3.81		
		3.64		

A plot of the measured intensity decrease for the different sample fibres is presented in Fig.3.9. Because of the large standard deviation obtained, it is difficult to tell if there is a linear relationship between the fibre dimensions and the registered intensity decrease. With improved spectral resolution, one would probably be able to draw more accurate conclusions.

In Fig. 3.10a time-traces of the photodiode output voltage at stable lasing conditions are shown. As can be seen, there are several "stable" levels characterized by low noise and a lifetime of several minutes. (The lower semi-stable level is somewhat noisier.) However, the highest intensity levels were extremely difficult to reproduce. In this particular case, the intensity difference between the higher and the lower stable level was 13.5%. (It should be compared with the recorded fibre signals (at most 4%) described in Sect. 3.2.)

Fig 3.7 *Plot of the measured output light intensity decrease caused by a fibre located inside the external cavity beam. We define it as the inner cavity signal. The square markers correspond to measurements on: glass fibre (5.6 μm); kevlar fibre (12 μm); twisted carbon fibre (14 μm); nylon fibre (34 μm).*

Table 3.3 *The measured output light intensity decrease caused by a fibre located inside the external cavity beam, here defined as the inner cavity signal.*

Fibre sample	Fibre dimension (μm)	Light intensity decrease (%)	Mean value (%)	Standard deviation (%)
glass fibre	5.6	0.42	0.38	0.04
		0.34		
		0.39		
twisted carbon fibre	14	1.05	1.19	0.15
		1.19		
		1.34		
kevlar fibre	12	0.18	0.53	0.31
		0.65		
		0.76		
nylon fibre	34	1.55	1.63	0.12
		1.57		
		1.76		

At unstable lasing conditions, the light output becomes very noisy with statistically distributed intensity breakdowns as depicted in Fig. 3.10b. The output optical power oscillated then between the two stable levels.

Fig. 3.11 contrasts the recorded light spectra emitted by the laser diode at stable lasing conditions and at "coherence collapse" (see Sect. 2.1.2). At unstable conditions some subsidiary longitudinal modes boost the intensity and multi-mode emission eventually develops.
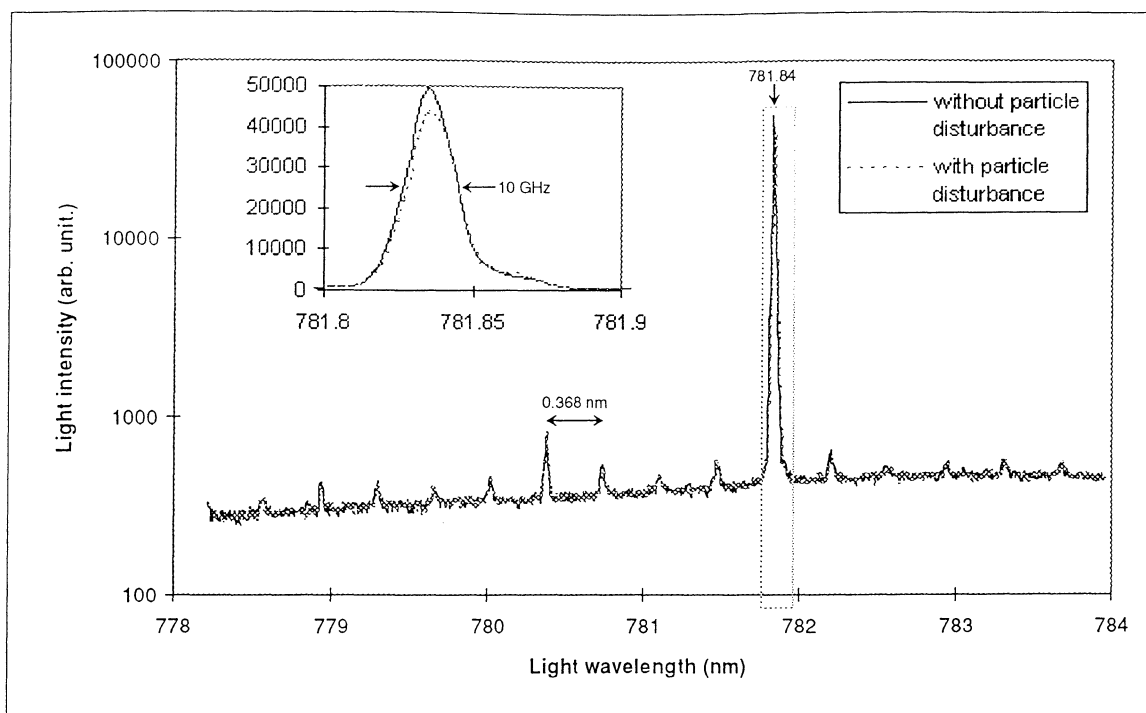
Fig. 3.8 *Recorded spectra of the emitted laser light without particle disturbance (solid line), and with a fibre located in the external cavity (dashed line). The towering peak at 781.84 nm is the single-mode line of the compound cavity lasing system, while the smaller peaks correspond to longitudinal modes of the laser diode cavity. The effect of the fibre disturbance is that the intensity of light at the single-mode peak is reduced (see enlarged graph). Notice the logarithmic intensity scale in the main graph, used to emphasise the faint longitudinal modes. The intensity offset is due to external stray light and electronical dark current.*
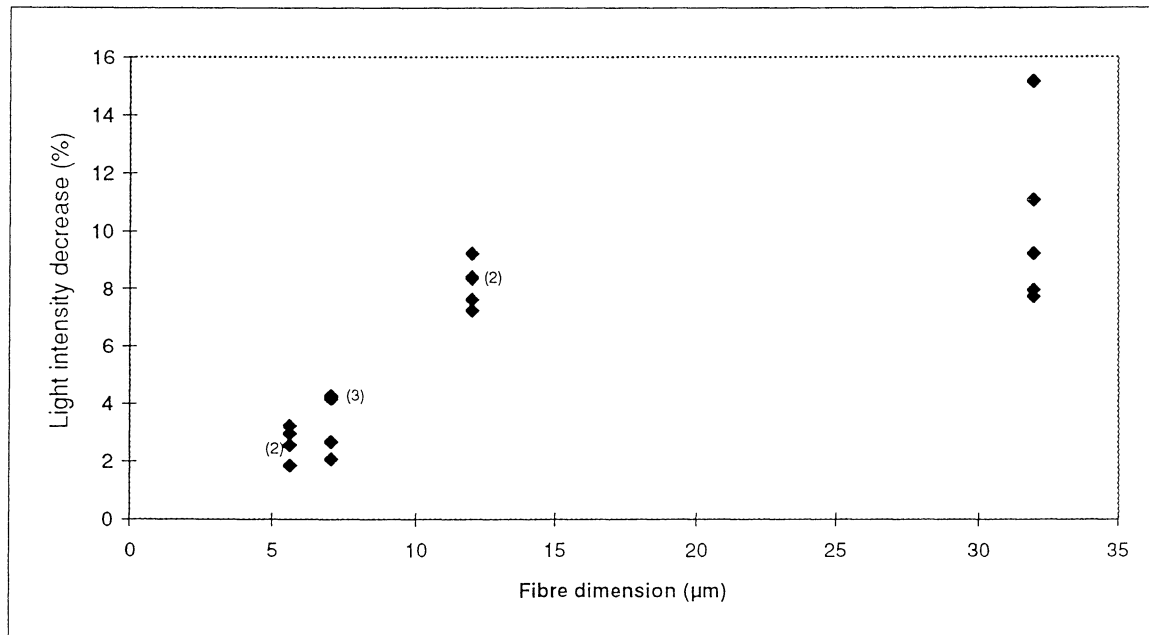
Fig. 3.9 *Plot of the light intensity decrease, measured with the spectrometer CCD camera at the single-mode wavelength, versus the fibre dimension (see also inset in Fig. 3.8). The square markers correspond to measurements on: glass fibre (5.6 μm); carbon fibre (7 μm); kevlar fibre (12 μm); nylon fibre (34 μm). The attached figures indicate the number of overlapping markers, corresponding to different measurements.*
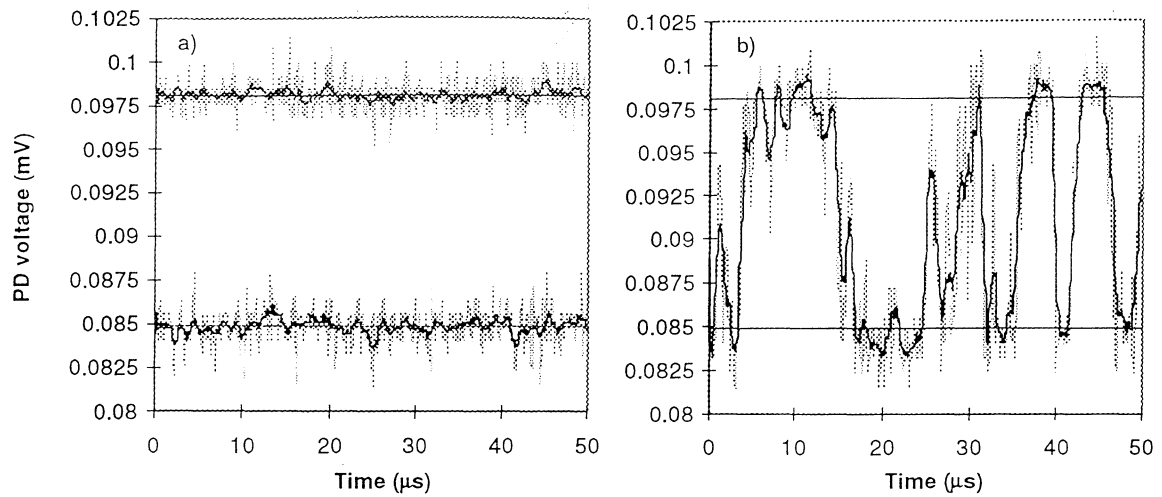
Fig. 3.10 *Time-trace of the photodiode (PD) output voltage, registered at semi-stable lasing conditions (a), and at coherence collapse (b). The two traces in graph (a) correspond to single-mode emission spectra. In this cases, the compound cavity system continued to be stable under several minutes. In graph (b) the output light intensity becomes very noisy and shows breakdowns, as it oscillates between the two stable levels (straight lines). Spectra corresponding to stable respectively coherence-collapsed conditions are shown in Fig. 3.11.*
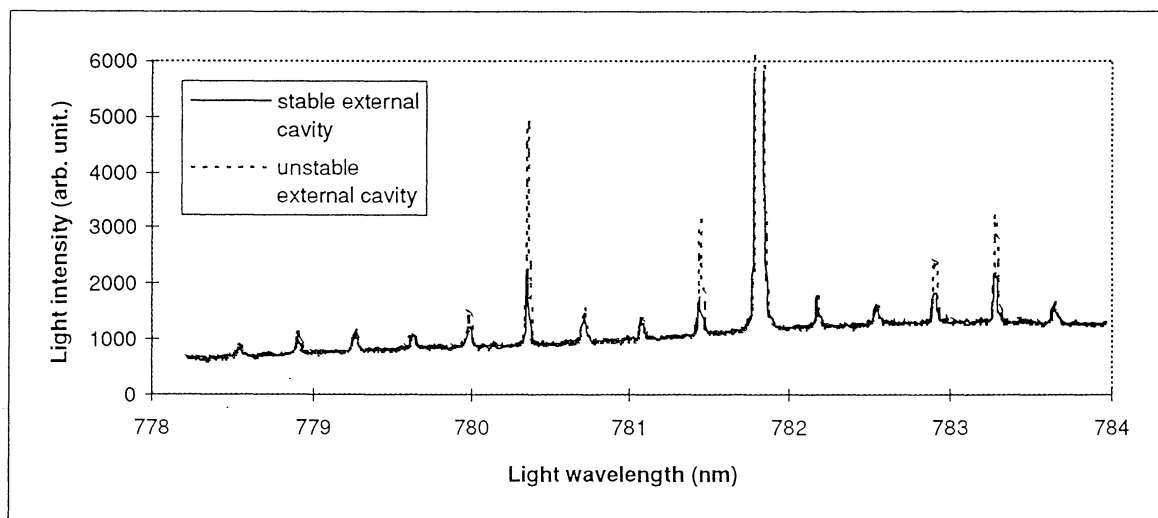
Fig. 3.11 *Recorded spectra of the emitted laser light, registered at stable lasing conditions (solid line), and at coherence collapse (dashed line). Notice the strong intensity increase of the longitudinal diode cavity modes, eventually leading to a multi-mode lasing behaviour. The linear intensity scale was zoomed for clarity of presentation.*

4. Discussion and conclusions

4.1 Comments on the measurements and on the results

A few remarks on the measurements and on the obtained results follow below.

The diffraction pattern. The broadening of the diffraction pattern (see Fig. 3.1) is probably caused by aberrations introduced by the imaging optics. Laser light incoherence can be ruled out as the source of broadening, since no discernible difference in image quality was registered between single-mode and multi-mode lasing conditions. The arrangement of the lenses L2 and L3 has been experimentally tested and theoretically evaluated in order to minimise the spherical aberrations, and the optimal arrangement was consequently chosen as shown in Fig. 2.7.

Due to insufficient spatial filtering by the spot dump (see Fig. 2.8), and a slight off-axis position of the imaging lenses L2 and L3, the intensity distribution exhibits some non-uniformities on the edge of the central blocked region, and is asymmetrically truncated by the collecting optics.

Very small particles scatter light at a wide angle. Hence, the limit for the smallest detectable particle size using the diffraction analysis method, is given by the collecting angle range and the magnification rate of the optics (alternatively the size of the CCD imaging chip).
As an upper limit, diffraction from large particles is concentrated at very small angles near the axis of the illuminating beam. In this case, the resolution of the CCD camera acts as the limiting factor.

After a particle leaves the beam, there is a brief period during which the diffraction image is saved, the trigger is reactivated, and other housekeeping procedures are completed. During these periods, the sensor cannot detect particles entering the sensing volume. The response time of the electronics, e.g. the sensitivity of the monitoring CCD camera or the speed of the frame grabber, is determining the maximum rate at which diffraction pattern recordings can be done.

The output light intensity. The laser beam displays an essentially Gaussian intensity profile with superposed interference fringes (see Fig. 2.4). This spatial variation of light intensity across the sensing volume, should have a quite significant effect on the particle measurements. It may lead to a dependency of the registered signals on the aerosol particle's trajectory through the beam.

By careful examination of the recorded intensity signals from multiple consecutive samplings shown in Fig. 3.4, it can be noticed that in some cases the edge signals become smaller at the second and third sampling. This is probably due to an experimental artefact, caused by insufficient removal of the fibre between consecutive samplings. (The fibres were translated by hand up and down through the sensing volume.) It is significant to observe, however, that the inner cavity signals remain apparently constant.

Some of the variations of the signal amplitudes at sampling of the same fibre could be attributed to non-uniformities and surface roughness of the measured fibres. This should be true especially for the nylon fibre, which presented great variations in thickness.

The signal-to-noise-ratio (SNR) is a limiting factor which must be improved in order to make possible detection of very small particles. The smallest particle which can be measured with the present set-up may be inferred from the plot in Fig. 3.6. The standard deviation of the recorded output, here defined as the output noise, was averaged to 0.21%. Thus, with a signal-to-noise-ratio SNR = 1 (SNR = signal amplitude/noise amplitude) the smallest detectable fibre diameter is $\approx$ 2 μm.

4.2 Conclusions

A simple and inexpensive measurement method for aerosol particle characterization using low-angle scattering is presented. It is based on the use of a semiconductor laser coupled to an external cavity, a built-in photodiode, a monitoring CCD camera, an oscilloscope, and conventional optics.

The near-forward-scattering technique minimises (but do not eliminate) refractive index effects, so that information about the size and the shape of the aerosol particles can be derived from the collected diffraction pattern. The derived values of the fibre diameters obtained assuming Fraunhofer diffraction showed good agreement, within the accuracy of the measurement, with the measurements made under the microscope.

From the time-resolved recording of the output optical intensity, the number and the velocity of the aerosol particles have been derived. Especially, it was found that the light intensity decrease as a fibre enters or leaves the sensing volume is linearly proportional to the fibre size. This edge phenomenon is attributed to the effect of particle diffraction. As the particle is moving well inside the sensing volume, the light absorption provides information about the refractive index of the particle material.

The two measurement components which are employed by the detector, i.e. sampling of scattered light in the near-forward direction and monitoring of output intensity variations, complement each other well. For instance, the refractive index and the velocity of the particle do not affect the diffraction pattern distribution, but these particle parameters can be evaluated using the time-resolved variation of the output intensity. The scattering pattern provides information about the shape of the particle and can therefore be used as a "fingerprint" for particle identification (by comparison with reference data).

The detecting range of the present instrument is evaluated to be between 2 μm and 100 μm.

It was experimentally found that control of the mechanical stability and possibility to very fine adjustments are crucial for the stable operation of the system. The operating current of the semiconductor laser was chosen below the solitary laser threshold. In this case, coherent optical interference between the field inside the laser diode and the light reflected from the external mirror makes the system to function as a compound cavity system. The intensity output is then stable and the optical spectrum is single-mode.

A theoretical treatment of the particle disturbance in the external cavity is proposed, in which the boundary-value problem at the feedback-coupling laser facet is solved. Thereby an expression for the so called effective mirror reflectivity $R_{eff,p}$ is derived, which can be used to evaluate the output power variation in the presence of an aerosol particle inside the external cavity.

The proposed measuring technique can be used in applications such as ambient air studies or in working environment hygiene, e.g. for monitoring and identifying trace quantities of hazardous materials in the air.

The small size of the semiconductor laser and the very low optical power emitted (≈ 100 μW) should be emphasised, because it opens the door for a future miniaturisation of the device. Driven by an ordinary battery, and made very compact with the use of GRIN (gradient index) lenses and optical fibres, the optical sensor cold be employed for instance in continuous recording of exposure to hazardous aerosol particles close to the mouth during the whole course of a breathing cycle.

The experimental findings are quite promising, and call for continued research in applying active scattering in external cavity coupled semiconductor lasers for the detection of aerosol particles.

5. Acknowledgements

I feel fortunate to have been given the opportunity to work with this project, which contained such a broad spectrum of theoretical and applied physics and which focused on an area of major concern and importance: *environmental research*. It was also stimulating to work with the professional and friendly staff at the Atomic Physics Department, and I feel very grateful for all support that I got.

First, I would like to thank Jonas Sandsten for his guidance, and for never sparing his time to help me in the everyday work. During this time, we have had many fruitful discussions, and I learned a lot about practical research work from him.

I am also grateful to Sune Svanberg for giving me the possibility to work with this project, and for all generous help and support. With his boundless enthusiasm and commitment, he is a true inspirer in my studies of physics.

I would also like to thank Ulf Gustafsson for the kind help he always offered me, especially by dealing with computer problems. His good advise spared me many hours trying to cope with software subtleties.

I thank Jan Hultquist, from the mechanical workshop, for all the brilliantly executed mechanical details, and to Petter Weibring for the good advise, encouragement, and for good company.

Finally, I am very thankful to Åke Bergquist, Hans Edner, and Anders Persson, for their invaluable help dealing with various practical problems encountered during the work with this project.

6. References

1. C.D. Ahrens, *Meteorology Today*, Fifth Edition, West Publishing Company (1994).

2. K. Willeke and P. A. Baron, *Aerosol Measurement — Principles, Technics, and Applications*, Van Nostrand Reinhold, New York (1993).

3. S. Svanberg, *Atomic and Molecular Spectroscopy — Basic Aspects and Practical Applications*, Second Edition, Springer-Verlag (1992).

4. R.M. Measures, *Laser Remote Sensing — Fundamentals and Applications*, John Wiley & Sons (1983).

5. S. Svanberg, *Real-World Applications of Laser Spectroscopy*, Optics & Photonics News, September (1996).

6. O. Graydon, *Scattering Patterns Reveal Asbestos Fibres*, Opto & Lasers Europe, July (1997).

7. S. Borgström, *Laserteknik*, KF-Sigma Lund (1994).

8. K. Petermann, *Laser Diode Modulation and Noise*, Kluwer Academic Publishers, Dordrecht (1988).

9. J. Hecht, *The Laser Guidebook*, Second Edition, McGraw-Hill, New York (1992).

10. S.M. Sze, *Semiconductor Devices — Physics and Technology*, John Wiley & Sons (1985).

11. B. Mroziewicz, M. Bugajski, and W. Nakwaski, *Physics of Semiconductor Lasers*, Polish Scientific Publishers, Warszawa (1991).

12. K. J. Ebeling, *Integrated Optoelectronics — Waveguide Optics, Photonics, Semiconductors*, Springer-Verlag (1993).

13. J.H. Osmundsen and N. Gade, *Influence of Optical Feedback on Laser Frequency Spectrum and Threshold Conditions*, IEEE Journal of Quantum Electronics **19**, 465-469 (1983).

14. R. Lang and K. Kobayashi, *External Optical Feedback Effects on Semiconductor Injection Laser Properties*, IEEE Journal of Quantum Electronics **16**, 347-355 (1980).

15. L. Viana, S. S. Vianna, M. Oriá, and J. W. R. Tabosa, *Diode Laser Mode Selection Using a Long External Cavity*, Applied Optics **35**, 368-371 (1996).

16. J. Kato, I. Yamaguchi, N. Kikuchi, and S. Ozono, *A Multi-Dimensional Displacement Sensor Using the Optical Feedback of Laser Diodes*, SPIE Vol. 1553, 23-32 (1991).

17. J. Sigg, *Effects of Optical Feedback on the Light-Current Characteristics of Semiconductor Lasers*, IEEE Journal of Quantum Electronics **29**, 1262-1270 (1993).

18. H. Kakiuchida and J. Ohtsubo, *Characteristics of a Semiconductor Laser with External Feedback*, IEEE Journal of Quantum Electronics **30**, 2087-2097 (1994).

19. A. Olsson and C.L. Tang, *Coherent Optical Interference Effects in External-Cavity Semiconductor Lasers*, IEEE Journal of Quantum Electronics **17**, 1320-1323 (1981).

20. R.P. Salathé, *Diode Lasers Coupled to External Resonators*, Applied Physics **20**, 1-18 (1979).

21. H.C. van de Hulst, *Light Scattering by Small Particles*, Dover Publications, New York (1981).

22. G. Mie, Ann. D. Physik **25**, 377-442 (1908).

23. L.V. Lorenz, Vidensk. Selsk. Skr. **6**, 1-62 (1890).

24. S. Hayashi, *A Laser Small-Angle Scattering Instrument for the Determination of Size and Concentration Distributions in Sprays*, Liquid Particle Size Measurement Techniques: 2nd Volume, American Society for Testing and Materials, 77-92, Philadelphia (1990).

25. P.G. Felton, *A Review of the Fraunhofer Diffraction Particle-Sizing Technique*, Liquid Particle Size Measurement Techniques: 2nd Volume, American Society for Testing and Materials, 47-59, Philadelphia (1990).

26. E. Hecht and A. Zajac, *Optics*, Second Edition, Addison-Wesley Publishing Company (1974).

27. H. Hinrikus and K. Meigas, *Laser Doppler Device for Air Pollution Detection*, SPIE Vol. 2271, 150-159 (1994).

28. P. Besnard, B. Meziane, and G.M. Stéphan, *Feedback Phenomena in a Semiconductor Laser Induced by Distant Reflectors*, IEEE Journal of Quantum Electronics **29**, 1271-1284 (1993).

29. R. Akselsson, M. Bohgard, A Gudmundsson, H-C. Hansson, B. Martinsson, B. Svenningsson, *Aerosoler*, Lunds Tekniska Högskola och NOSA (1994).

30. S-G. Petterson, S. Borgström, and H. Hertz, *Advanced Optics*, KF-Sigma Lund (1994).

31. D. M. Kane and A. P. Willis, *External-Cavity Diode Lasers with Different Devices and Collimating Optics*, Applied Optics **34**, 4316-4325 (1995).

32. D.R. Lide, *Handbook of Chemistry and Physics*, CRC P (1995).

33. D-S. Seo, J-D. Park, J. G. McInerney, and M. Osinski, *Multiple Feedback Effects in Asymmetric External Cavity Semiconductor Lasers*, IEEE Journal of Quantum Electronics **25**, 2229-2237 (1989).

34. Y. Kitaoka, H. Sato, K. Mizuuchi, K. Yamamoto, and M. Kato, *Intensity Noise of Laser Diodes with Optical Feedback*, IEEE Journal of Quantum Electronics **32**, 822-827 (1996).

7. Appendices

A. Development and test of the experimental set-up

During the development of the optical aerosol sensor, an extensive series of tests was conducted in order to evaluate the optimal experimental arrangement and the best set of components.

Different types of commercial laser diodes were studied. Apart from tests on the near-infrared emitting laser Sony SLD114VS (which was found to have the best optical properties), another infrared diode laser (Sharp LT010MDO, $\lambda = 820$nm) and a red multi-quantum-well laser (Sony SLD1133VL, $\lambda = 650$nm) were examined. There was also a considerable variance of the output light properties of devices of the same type, so one could say that all laser diodes are individuals.

The output beam profile is depending on the collimating lens in use. Two gradient index (GRIN) Selfoc® collimating lenses (SPL AG3645-2 and SLW-300 S11078-C2), a Newport microscope lens, and a moulded glass aspherical lens (Geltech 350230) were used to collimate the divergent laser emission. Although GRIN lenses have many advantages (they have only two surfaces which can reflect unwanted feedback light and are producing the narrowest collimated beam), they distorted the output wave front due to poorer optical quality. The Geltech collimating lens yields the best beam quality and delivers a relatively narrow beam.

Different lens arrangements have also been tested. The major problem consisted in reducing the spherical aberrations which impaired the quality of the diffraction image.

B. Improvement suggestions

Some improvements of the experimental set-up are suggested here.

The primary laser beam should be totally filtered from the scattered light of the particle in order to improve the diffraction image quality. This could be done effectively by using a beamsplitter with a hole, placed at the focus of the transform lens L1. The primary laser light would then pass through the hole without being reflected onto the CCD camera.

A large aperture of the Fourier transform lens (alternatively a shorter focal length of this lens) would increase the solid angle for the collected scattered light, enabling analysis of diffraction patterns from very small particles.

Serious problems arise in practice because of unintentional external feedback. Undesired feedback from the imaging optics can be avoided by antireflection coating all the lenses. The plane external mirror should be replaced by a wedge (eventually AR-coated) to limit the external feedback to only one reflecting surface (compare with Sect. 2.1.2).
In order to improve the coupling to the external cavity, the diode mirror facing the external reflector could also be antireflection coated.

The external cavity length can be finely controlled by inserting a piezo-electric transducer disk between the adjustment screws and the movable part of the external mirror mount.

Mechanical vibrations, which cause significant unwanted disturbance on the sensitive detector system, must be satisfactorily isolated. The whole experimental set-up should be isolated from the floor, for instance by placing it on pieces of soft rubber.

To avoid massive air flows into the cavity, passive sampling may be performed. Natural air convection or settling under the influence of gravity can then be used to transport the aerosol particles into the sensing volume of the instrument.

With a Millikan device based on the electrodynamic balance, single irregular particles can be suspended in the sensing volume of the detector so that the variation of the diffraction pattern and the output intensity signals for all possible orientations of the particle can be readily studied.

An exact quantitative analysis requires a calibration of the optical sensor. By presenting well-characterized aerosol particles to the instrument and by varying one particle-parameter at a time (i.e. the size or the refractive index) the instrument response can be compared with the known result. The sensor should also be calibrated against other aerosol measuring instruments in order to verify its performance. The crucial instrument properties with regard to particle sizing are: precision (repeatability), accuracy (resolution), sensitivity (lowest detectable size), and dynamic range.

Additionally, a numerical simulation of the theoretical model for the interaction between the aerosol particle and the electromagnetic field inside the external cavity (see Sect. 1.5) could be useful for interpreting the experimental data.

Derivation of fibre dimensions using the extrema positions in the experimentally recorded diffraction pattern. (Compare with Fig.3.1, Fig. 3.2)
Fraunhofer diffraction approximation is assumed.
Δ = distance between two succesive minima, estimated by paring corresponding extrema. (The values for the maxima have been appropriately adjusted.)

	Scale (mm/pixel)	Wavelength (nm)
	0.0135	781.84

Single carbon fibre:

	min/max position (pixel)	Δ (pixel)	Mean value (pixel)	Standard deviation (pixel)	Variance (pixel)	Mean value (mm)	$\Theta 1$ (°)	Fibre thickness (µm)		Accuracy (µm)
1st max	43.56	110.6	111.0	0.5597	0.313	1.498	0.1119	**7.00**	±	**0.04**
1st min	92.30	111.4		Std. dev. (mm)						
1st min	315.01			0.00756		1.506	0.1124	6.97		
1st max	359.85					1.490	0.1113	7.04		

Twisted double carbon fibre:

	min/max position (pixel)	Δ (pixel)	Mean value (pixel)	Standard deviation (pixel)	Variance (pixel)	Mean value (mm)	$\Theta 1$ (°)	Fibre thickness (µm)		Accuracy (µm)
3rd min	31.55	52.33	52.69	0.5146	0.265	0.711	0.0533	**14.67**	±	**0.14**
2nd max	60.51	52.21								
2nd min	82.12	53.29		0.00695		0.718	0.0538	14.53		
1st max	113.64	52.95				0.704	0.0528	14.82		
1 st min	135.24									
1st max	265.11									
2nd min	295.29									
2nd max	317.25									
3rd min	345.52									
3rd max	366.94									

Kevlar fibre:

	min/max position (pixel)	Δ (pixel)	Mean value (pixel)	Standard deviation (pixel)	Variance (pixel)	Mean value (mm)	$\Theta 1$ (°)	Fibre thickness (µm)		Accuracy (µm)
3rd min	22.54	55.89	55.14	1.0646	1.133	0.744	0.0558	**14.03**	±	**0.28**
2nd max	55.82	54.12								
2nd min	79.19	54.34		0.01437		0.759	0.0568	13.76		
1st max	110.35	56.22				0.730	0.0547	14.30		
1 st min	129.28									
1st max	271.16									
2nd min	296.54									
2nd max	321.98									
3rd min	357.86									

Nylon fibre:

7th max	23.72	22.37	22.35	0.4576	0.209	0.302	0.0226	**34.56**	**±**	**0.72**
7th min	37.06	21.81							
5th min	76.02	22.92		0.00618		0.308	0.0231	33.87	
4th max	91.21	22.28				0.296	0.0222	35.29	
4th min	103.69								
3rd max	111.91								
3rd min	121.45								
2nd max	136.51								
2nd min	147.59								
4th max	290.75								
5th min	305.27								
7th min	342.37								
7th max	358.68								
8th min	375.66								
8th max	394.20								